

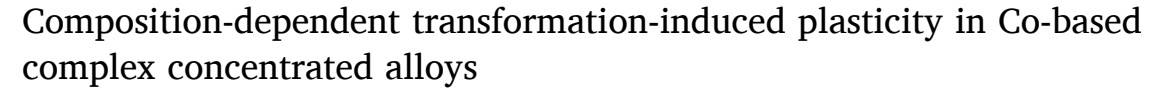
Contents lists available at ScienceDirect

# Acta Materialia

journal homepage: www.elsevier.com/locate/actamat



# Full length article



Hyun Seok Oh, Michael Xu, Shaolou Wei, Felicity F. Worsnop, James M. LeBeau, C. Cem Tasan

Department of Materials Science and Engineering, MIT, 77 Massachusetts Avenue, Cambridge, MA 02139 United States of America

#### ARTICLE INFO

Keywords:
Complex concentrated alloy
Negative stacking fault energy
Nitrogen
Faulting-induced plasticity
Transformation-induced plasticity

#### ABSTRACT

While the mechanically-induced martensitic transformation and transformation-induced plasticity (TRIP) effects have various known benefits, transformation of blocky martensite can also accelerate ductile damage nucleation and growth. Some complex-concentrated alloys (CCAs) with negative stacking-fault energy (SFE) demonstrate a rare faulting plasticity behavior with high strain hardening capability, that sets them apart from conventional low, positive SFE alloys that exhibit the TRIP effect. This study investigates the influence of dilute nitrogen on the TRIP mechanisms in a Co-rich CoCrNi CCA, and reveals, among other findings, that nitrogen interstitials can effectively reduce the extension of stacking faults and deformation-induced phase transformation, resulting in higher strain hardenability at early deformation levels and ductility. Thermodynamic calculations are coupled to various experimental analyses based on atom-probe tomography, scanning transmission electron microscopy, electron backscattered diffraction, electron-channeling contrast imaging, *in situ* high-energy synchrotron X-ray diffraction, and stress relaxation testing, to explore the origins of the observation. This work provides insights into the future design of CCAs with desirable TRIP, faulting plasticity, and mechanical properties.

#### 1. Introduction

Single-phase face-centered cubic (fcc) complex concentrated alloys (CCAs) have attracted attention due to their promising mechanical properties [1–4]. The complex atomic environment in these alloys can diversify the underlying strengthening mechanisms, ranging from solid-solution strengthening to chemical short-range ordering [1,3,5]. This enables tunable load-bearing performance at ambient and cryogenic temperatures. In this regard, plasticity micro-mechanisms are of fundamental importance: with decreasing intrinsic stacking fault energy ( $\gamma_{iSFE}$ ), the dominant deformation modes in fcc-structured CCAs can vary from perfect dislocation slip to twinning-induced plasticity (TWIP), and to transformation-induced plasticity (TRIP) [5,6]. An appreciable amount of literature has successfully uncovered the correlation amongst composition,  $\gamma_{iSFE}$ , and mechanical properties, presuming a positive  $\gamma_{iSFE}$ . On the other hand, theoretical and experimental investigations of CCAs with negative  $\gamma_{iSFE}$  remain limited, which motivates the present study.

It is widely accepted that TRIP is the major plasticity mechanism in alloys with low SFEs, such as medium or high Mn-steels with SFE<20 mJ/m $^2$  [7]. This is because a low SFE indicates that the parent *fcc* phase

is mechanically metastable and favors displacive transformation during plastic deformation (i.e., deformation-induced phase transformation DIPT) [7,8]. However, some studies have reported plasticity behavior primarily mediated by stacking faults, in lieu of DIPT—a phenomenon we term faulting plasticity here—in CCAs with negative  $\gamma_{\rm ISFE}$ , such as Cu-Al [9,10], CoCrMoN [11] and CoCrNiW [12]. This mechanism provides new opportunities for CCA design, as blocky martensite is prone to damage due to limited slip systems and plastic strain incompatibility [12–14].

Regarding its origin, Yamanaka et al. [11] proposed that nanoscale  $Cr_2N$  and SRO associated with Cr-N bonding function as obstacles to the glide of Shockley partials and suppress the DIPT in CoCrMoN. Another origin was proposed by some of the authors of this study, in Wei et al. [12], focusing on SFE. Through *in situ* electron channeling contrast imaging (ECCI) tests, it was shown that the formation of mono-layered stacking faults (SFs) can be energetically favored in CoCrNiW with negative  $\gamma_{iSFE}$ . This enables the formation of uncorrelated SFs during early-stage deformation, thereby delaying the formation of more stable bulk structures (e.g., hexagonal close-packed (hcp) phase or twin). Further, Pei et al. [15] demonstrated through the density-functional theory (DFT) calculations that two Shockley partials can even switch

E-mail address: tasan@mit.edu (C.C. Tasan).

<sup>\*</sup> Corresponding author.

their positions, forming an fcc stacking between the two SFs instead of a wide SF. All these studies thus support the possibility of the faulting plasticity in CCAs with negative  $\gamma_{iSFE}$ . Yet, a recent molecular dynamics study suggested that SRO and solute fluctuation in CrCoNi are insufficient to kinetically hinder the thermal activation of partial dislocations at room temperature [16], implying negligible effects of SRO on the extension of stacking faults and the resultant DIPT.

It is thus essential to understand which nanoscale chemical heterogeneities can effectively reduce martensitic transformation and increase the contribution of stacking faults on plasticity, without relying on longrange ordered precipitates. To this aim, doping interstitial elements can be a promising candidate. A recent nanoindentation study on FeMn-CoCrCN suggested that nitrogen atoms can trap partial dislocations [17]. This result implies that the interstitial atoms, which are weaker obstacles compared to long-range ordered precipitates, can effectively reduce the width of SFs and suppress DIPT. It is thus imperative to understand the effects of interstitial elements on active mechanisms of deformation faulting and DIPT to use the information for further design of CCAs with the faulting plasticity mechanism. However, interstitial elements have diverse effects on plasticity, posing challenges to study. Interstitial elements can change the chemical Gibbs energy of each phase and SFE, which has been actively studied in high-manganese steels [7] and austenitic stainless steels [18,19]. Interstitial elements can also form interstitial SROs with other substitutional elements, which can hinder dislocation motions [11,20]. As SRO can alter local SFEs in CCAs [2], the formation of interstitial SROs is also expected to cause fluctuation in local SFEs. Additionally, interstitial elements can segregate to dislocation cores, causing dynamic strain aging or changing SFE of SFs (i.e., Suzuki segregation) [21,22]. This effect typically occurs at high temperatures where the diffusivity of interstitial elements is high. However, a recent study showed that interstitial elements can accumulate in refractory metals even near 0 K without long-range diffusion [23], implying the possibility of their accumulation in fcc CCAs due to plastic deformation.

This present work aims to examine the potential of interstitial elements on TRIP, particularly focusing on suppressing DIPT and promoting SFs. To this end, we select a Co-rich CoCrNi CCA that exhibits a theoretical  $\gamma_{iSFE}$  of -44 mJ/m<sup>2</sup> as a model system and examine the effects of doping 0.2 at.% nitrogen (N). The microstructure and defect evolution during uniaxial tensile deformation in Co-rich CoCrNi samples with or without N (CCN-N and CCN) are firstly characterized via the combination of electron-back scattered diffraction (EBSD) and electronchanneling contrast imaging (ECCI) probing in the scanning electron microscopy (SEM) and in situ high-energy X-ray diffraction (HEXRD) testing. We then discuss the effects of N on deformation faulting in detail taking into account  $\gamma_{iSFE}$ , SRO, segregation, and pinning through structural and mechanical characterization methods, including atom-probe tomography (APT), scanning transmission electron microscopy (STEM), and repeated stress relaxation tests. The results indicate that CCN and CCN-N exhibit different TRIP behaviors that N effectively hinders the extension of SFs, leading to the formation of discrete SFs and nano-hcp phase, and reducing DIPT into the hcp phase. By examining these alloys with a minimal nitrogen content, we envision further advancements to fully suppress DIPT, enabling deformation exclusively via SFs, paving the way for the development of damage-tolerant CCAs.

## 2. Experimental methods

## 2.1. Fabrication

The samples with nominal composition  $Co_{44.4}Cr_{33.3}Ni_{22.2}$  (at.%, CCN) and  $(Co_{44.4}Cr_{33.3}Ni_{22.2})_{99.8}N_{0.2}$  (at.%, CCN—N) were produced by arc melting using high-purity elements (Cr, Co, Ni, and CrN; purity > 99.9%) under Ti-gettered Argon atmosphere. The nitrogen content in CCN—N was measured by the infrared combustion method (Laboratory Equipment Corporation, LECO), and the impurity N content in CCN is

expected to be 0.05 at.%. The alloy buttons were re-melted more than five times to improve the compositional homogeneity. The buttons were then cast into a water-cooled copper mold with a rectangular cavity (=20 mm width  $\times$  8 mm thickness  $\times$  60 mm length). The as-cast ingots underwent hot rolling to a final thickness of 2 mm (~75% thickness reduction) at 1273 K with intermediate annealing to maintain the temperature. The plates were then homogenized at 1473 K for 2 h in an Ar atmosphere, followed by water quenching to ambient temperature. The rolled sheets were further cold rolled to 1.1 mm (~45% thickness reduction) at room temperature and annealed at 1273 K for recrystallization (CoCrNi, 5 min; CoCrNi-N, 12 min), followed by water quenching to ambient temperature.

## 2.2. Characterization

#### 2.2.1. Microstructural characterization

The mesoscale microstructures of the samples were analyzed via electron backscatter diffraction (EBSD, EDAXZ Hikari camera), energy dispersive spectroscopy (EDS), and electron channeling contrast imaging (ECCI) using a Tescan MIRA 3 scanning electron microscope (SEM) operated at a voltage of 20 kV. The EBSD data were analyzed using the TSL OIM data-collection software. The specimens were mechanically ground and polished with Struers 1  $\mu m$  diamond suspension. The samples except for 5%-deformed samples were then electro-polished using diluted phosphoric acids with distilled water (85%) in an electro-polishing machine (Letropol, Struers). The 5%-deformed samples were polished in OPU suspension for  $\sim\!20$  min without electropolishing to ensure that the surface is flat enough for ECCI imaging.

#### 2.2.2. Synchrotron-based in situ high-energy X-ray diffraction

In situ synchrotron tensile tests were conducted at beamline 11-ID-C of the Advanced Photon Source, Argonne National Laboratory, USA. A schematic diagram of the experimental setup can be found in Fig. 2 in [12]. The dog bone-shaped specimens with a gage geometry of 10 mm (length)  $\times$  1 mm (thickness)  $\times$  1.5 mm (width) were subjected to tensile deformation at a nominal strain rate of  $1.0 \times 10^{-3}$  s<sup>-1</sup>, under the high-energy monochromatic X-ray beam (wavelength: 0.1173 Å, beam size: 500  $\mu m \times 500~\mu m$  ). The direction of the incident X-ray beam was perpendicular to the loading direction. The diffracted beam was recorded at every loading step on a two-dimensional large-area detector (PerkinElmer, quadratic pixel size of 200  $\mu$ m  $\times$  200  $\mu$ m) placed behind the sample. The distance between the sample and the detector was  $\sim$ 1500 mm. NIST-standard CeO $_2$  powder was used for calibration. The Rietveld refinement of the recorded ring patterns was performed using the Material Analysis Using Diffraction (MAUD) software [24] following the instruction in Appendix of Ref. [25]. The Popa LB, isotropic, diamond anvil cell (DAC) [26], and E-WIMV algorithms were used for line broadening, size-strain, and texture models, respectively. Exemplary patterns and the refinement results are presented in Fig. S1. The lattice strain was measured using the GSAS II software.

## 2.2.3. Atom probe tomography

The atom probe tomography (APT) samples were prepared using an FEI Helios 660 Dual-Beam Focused Ion Beam. The APT measurements were performed using a Cameca LEAP 4000 HR instrument in laserpulsing mode with a laser pulse energy of 75 pJ. The data analysis was performed using IVAS 3.8.4 software (CAMECA Instruments). The reconstruction was performed based on the tip profile.

## 2.2.4. Scanning transmission electron microscopy

Samples for scanning transmission electron microscopy (STEM) characterization were prepared by grinding foils to  $<\!50~\mu m$ , after which 3 mm discs were punched out. Ion milling (Fischione 1051) at 4, 3, 2, and 1 kV was performed to perforate and thin the discs. STEM imaging was performed using an aberration-corrected Thermo Fisher Scientific Themis Z 60–300 kV S/TEM using an accelerating voltage of 200 kV and

convergence semi-angle of 18.8 mrad. High-angle annular dark-field (HAADF) images were collected using a semi-angle of 65-200 mrad, and image series were taken and drift-corrected using the Revolving STEM (RevSTEM) method [27]. Analysis of short-range order utilized the methodology outlined in [28,29] in which atom column intensities are normalized and compared using a correlation template. The resulting correlated intensity map depicts areas of high order in atom column intensities. Statistically significant SRO is determined by spatial autocorrelation and local hotspot analysis using the local Getis-Ord Gi\* statistic with multiple hypothesis testing adjustments (analysis and visualization performed using the spdep and tmap packages in [30,31]). A cutoff value or z-score of 1.96 (p<0.05) is used as the threshold of clustering, after which contiguous ordered atom columns are grouped into individual SRO regions. Region properties for clusters with an area greater than four atom columns are then calculated and plotted. To avoid sampling issues, the distance from each cluster centroid to that of its three nearest-neighbors is used to determine the average distance.

#### 2.3. Mechanical property tests

#### 2.3.1. Tensile tests

Double-necked dog-bone specimens with 4 mm (length)  $\times$  1 mm (thickness)  $\times$  1.5 mm (width) gage geometry were prepared by electrical discharge machining (EDM) with the longitudinal axis perpendicular to the rolling direction. The specimens were ground using SiC abrasive papers and coated with a layer of white spray paint and a fine black speckle pattern of airbrushed ink. The specimens were subjected to tensile loading using a Deben Gatan MTest2000 miniature tensile stage at 40  $\mu m/s$  constant crosshead speed (10 $^{-3}$  s $^{-1}$ ). The surface patterns were recorded using an AlliedVision digital camera and VimbaViewer software. The macroscale strain was measured by digital image correlation (DIC) of the recorded surface patterns using the GOM correlate software. Three tensile tests were performed per sample.

## 2.3.2. Repeated stress relaxation test

Repeated load relaxation tests were conducted to measure the thermal activation volumes [32–34] at various plastic strain levels using an Instron 5984 testing machine. The tensile specimens with a dog-bone

shape and 20 mm (length)  $\times$  1 mm (thickness)  $\times$  3–4 mm (width) gage geometry were loaded with a strain rate of  $10^{-3}~\rm s^{-1}$ . At each desired plastic strain level, a stress relaxation cycle was repeated five times. A cycle consists of the relaxation period (i.e., the cross-head stopped for 30 s) and the reloading period (i.e., the specimens reloaded back to the initial stress level at the beginning of the relaxation). During relaxation, the load was recorded as a function of time. Two repeated load relaxation tests were performed per sample.

#### 3. Results

#### 3.1. Microstructure in the undeformed state

Fig. 1 presents the initial microstructures of CCN and CCN—N in the undeformed state. The EBSD inverse pole figure (IPF) maps show equiaxed recrystallized grain morphologies with average grain sizes of  $\sim\!19$   $\mu m$  in CCN (Fig. 1a1) and  $\sim\!23$   $\mu m$  in CCN—N (Fig. 1a2), excluding annealing twins. Both alloys mainly consist of an fcc phase (Figs. 1b1 and b2), with less than 0.5% hcp phase, as supported by HEXRD results (Fig. 1c1 and c2). The IPFs (Fig. S2) show that grains are randomly oriented in both samples. The lattice parameters of CCN and CCN—N are 3.5611 Å and 3.5627 Å, respectively. The EDS maps (Fig. S3) reveal uniform element distribution in both samples, at the resolution limit of SEM, except for oxide inclusions.

Fig. 1d1 and d2 show the thermodynamically predicted phase diagrams using Thermocalc (database: TCHEA3). The prediction matches the experimental results for CCN, as the recrystallization annealing temperature (1000 °C) falls in the high-temperature single fcc phase region. On the other hand, the calculation predicts the formation of a nitrogen-enriched hcp secondary phase (0.5% mole fraction) in CCN—N at 1000 °C, and the nitrogen content in the high-temperature fcc phase is only 0.04 at.%, which is lower than the nominal composition of nitrogen (0.2 at.%). Although not shown here, this is also predicted by different calculations using other databases (TCFE12, TCNI11) or different phase conditions (without the secondary phases).

To validate the thermodynamic prediction for CCN—N, the atomic-scale structure is observed using APT. Fig. 2a presents the reconstructed 3-D elemental atom maps of CCN—N. Most N atoms are

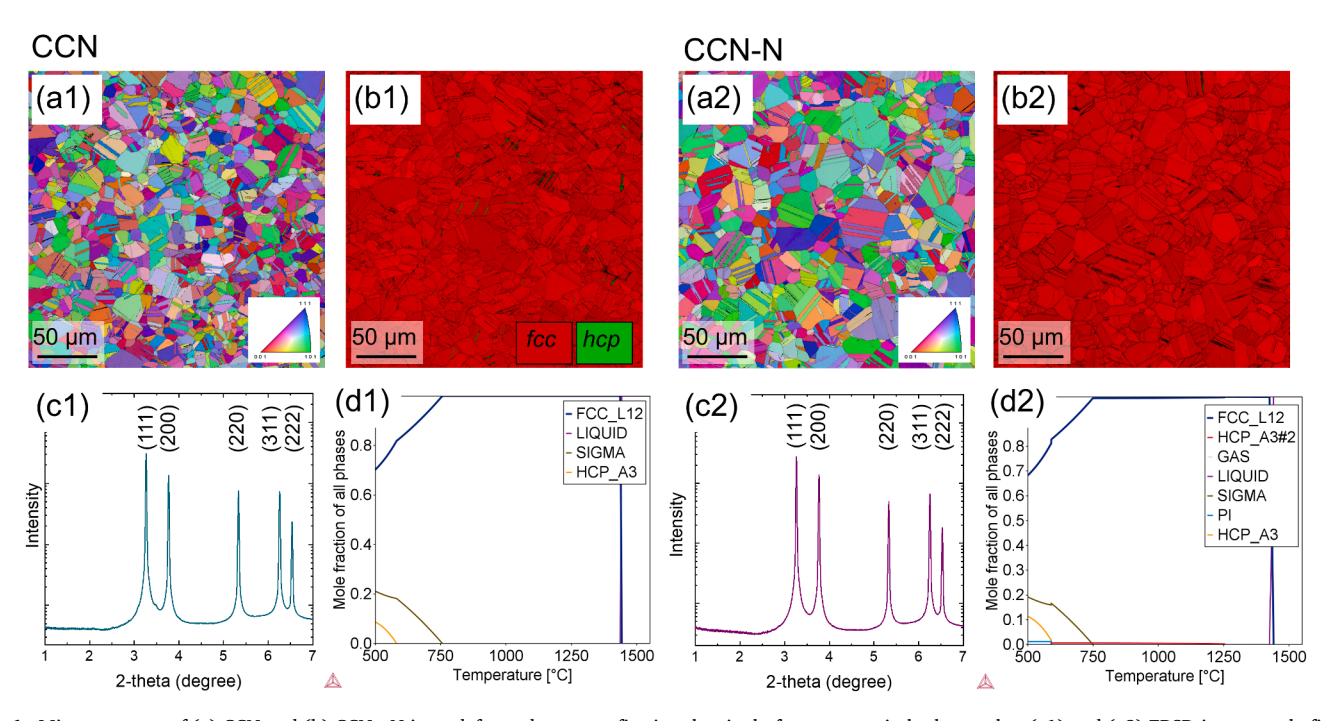


Fig. 1. Microstructure of (a) CCN and (b) CCN—N in undeformed state confirming the single fcc structure in both samples. (a1) and (a2) EBSD inverse pole figure maps. (b1) and (b2) EBSD phase maps. (c1) and (c2) HEXRD patterns. (d1) and (d2) Phase diagrams calculated as a function of temperature. EBSD step size: 350 nm.

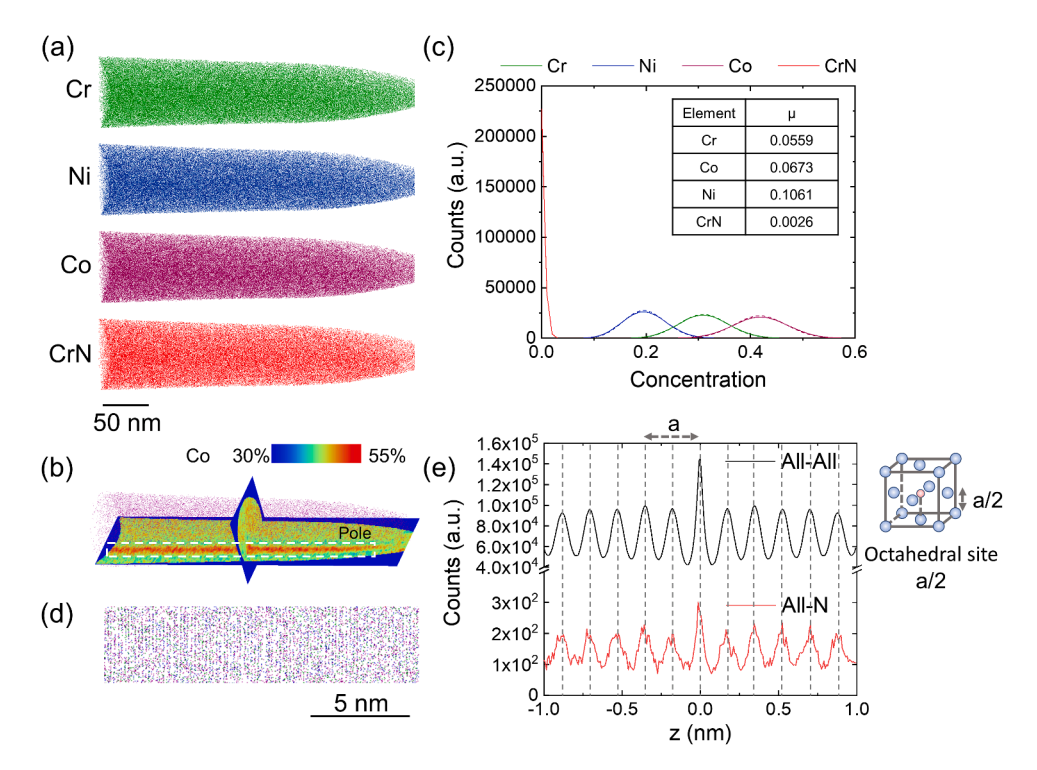


Fig. 2. APT results detected for a specimen of CCN—N. (a) Reconstructed 3-D atom maps showing the distribution of ion types. N was detected mainly within CrN complex ion. (b) 2-D contour plot of Co showing the crystallographic pole along a < 100 > direction. (c) Frequency distribution analysis outside the crystallographic pole. (d) Reconstructed 3-D atom map analyzed parallel to a  $\langle 100 \rangle$  direction, showing the atomic layer structure. (e) Spatial distribution analysis of all elements-all elements and all elements-N pairs. Dotted lines indicate the interplanar spacing.

detected in the form of CrN molecules. The APT tip was taken from the grain interior and does not include any grain boundaries. In the 2dimensional contour plot of Co (Fig. 2b), a crystallographic pole [35, 36] corresponding to the  $\langle 100 \rangle$  direction is observed, which originates from the differences in the evaporation field between Cr, Co, and Ni under the measurement conditions [37]. Thus, the pole does not imply chemical heterogeneity. There is no indication of compositional decomposition on the nm-scale outside the pole. Further, the frequency distribution analysis reveals a binomial distribution of all elements (Fig. 2c). The bulk chemical composition, as measured by the APT experiment, is listed in Table 1. The nitrogen content is 0.2 at.%, suggesting that all nitrogen atoms are dissolved in the matrix. By focusing on the crystallographic pole area (4 nm  $\times$  4 nm  $\times$  200 nm) (Fig. 2d), spatial distribution maps (SDMs) are calculated for N-all elements and all elements-all elements pairs (Fig. 2e). Both pairs exhibit the same interatomic spacing, indicating that nitrogen atoms occupy the octahedral sites of the fcc phase. Therefore, the APT results reveal the uniform distribution and full dissolution of N in the matrix in the resolution limit of APT, deviating from the thermodynamic prediction.

Fig. 3a displays the uniaxial tensile stress-strain curves of CCN and CCN—N. CCN exhibits 0.2% yield strength (YS0.2) of 420 $\pm$ 6 MPa, ultimate tensile strength (UTS) of  $\sim$ 904 $\pm$ 7 MPa, and uniform elongation (UE) of  $\sim$ 53 $\pm$ 1%. CCN—N exhibits YS0.2 of  $\sim$ 440 $\pm$ 14 MPa, UTS of  $\sim$ 943 $\pm$ 7 MPa, and UE of  $\sim$ 57 $\pm$ 0.5%. The strain hardening rate curves reveal that CCN—N has a higher strain hardening rate at true strain levels of 0–0.1 and 0.3–0.45. In summary, CCN—N has a higher UTS, UE, and strain hardening rate compared to CCN, although, the difference is not substantial.

**Table 1**Composition of CCN—N measured by APT.

Element	Cr	Co	Ni	N
Composition (at.%)	33.6	44.8	21.4	0.21

Fig. 4 presents the deformation substructures of CCN and CCN—N observed by ECCI at 5% strain. The microstructure images reveal planar features, which have characteristics of SFs or nano-hcp phase [12,38]. First, the planar features form along the {111} slip plane in both alloys (Fig. 4a1 and a2), as confirmed by the trace analysis carried out considering the loading direction and Euler angles using the STrCryst code [39]. Second, the planar structure has a sharp contrast on one side, and then the contrast fades through one direction (Fig. 4b1, b2, c1, and c2), which is a characteristic feature of SFs, separating them from twins [38]. Lastly, the bulky hcp phase or the characteristic misorientation change from deformation twinning (60) is not observed in the EBSD results with a 15 nm step size (Fig. 4d1, d2, e1, and e2). Further, considering the energetics of faulting, the formation of nano twins is unlikely. The activation barriers for twin fault, intrinsic SF, and hcp phase fault are  $\gamma_{USFE} - \frac{1}{2}\gamma_{ISFE}$ ,  $\gamma_{USFE}$ , and  $\gamma_{USFE}$ , respectively, where  $\gamma_{USFE}$  is unstable SFE [40,41]. Consequently, the negative  $\gamma_{iSFE}$  of the present CCAs would increase the activation barrier for twin fault compared to that of SF and hcp phase fault, suppressing twinning. Therefore, these planar features should be either SFs or nano-hcp phase finer than the resolution limit of EBSD, which is typically ~50 nm [38]; we will call this feature SF/nano-hcp here.

Both samples undergo plastic deformation through the formation of SF/nano-*hcp* at ~5% strain (Fig. 4a1 and a2). However, the patterns are different in terms of their extensions. CCN exhibits continuous SF/nano-*hcp* (Fig. 4b1) compared to CCN—N (Fig. 4b2). To make a systematic comparison, the patterns are divided into two categories as Continuous and Discrete. The former is when the SF/nano-*hcp* extends from one end to the other end of the grain, and the latter is when the SF/nano-*hcp* is narrower, ending in the middle of the grain; it is important to note that this does not imply that partial dislocations end in the middle of the grains. The pattern was analyzed in 50 individual grains using ECCI imaging, and the results are summarized in Figs. 4f1 and f2. Each dot on the map represents a grain. The red and green dots indicate grains with continuous SF/nano-*hcp* and discrete SF/nano-*hcp*, respectively. The

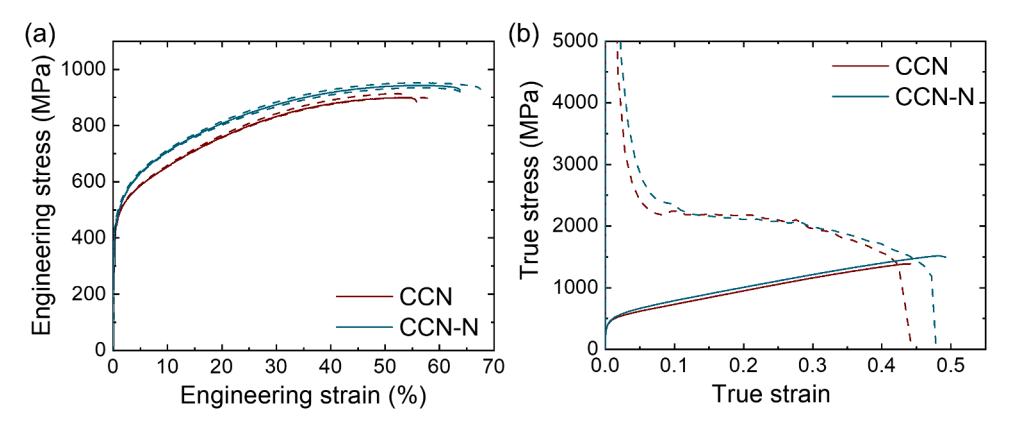


Fig. 3. Macroscopic mechanical properties of CCN and CCN-N. (a) Tensile stress-strain plots. (b) True stress-strain and strain hardening rate plots.

analysis shows that all grains in CCN have continuous SF/nano-hcp regardless of the crystallographic orientation. In contrast, 1/3 of the grains in CCN—N have discrete SF/nano-hcp. The grains close to  $\langle 001\rangle//\mathrm{ND}$  directions exhibit a higher propensity of discrete SF/nano-hcp, while those close to  $\langle 111\rangle//\mathrm{ND}$  directions mainly show continuous SF/nano-hcp. The orientation dependence of the faulting behavior can be explained by the difference in Schmid factors between the partial dislocations, which creates a difference in the shear stress acting on them, causing further extension of the SF [42–44]. Schmid factors are calculated for slip systems in grains with orientations close to  $\langle 001\rangle//\mathrm{ND}$ ,  $\langle 110\rangle//\mathrm{ND}$ , and  $\langle 111\rangle//\mathrm{ND}$  directions as an example in Table S1. The  $\langle 111\rangle//\mathrm{ND}$  orientation shows a larger Schmid factor difference (0.32), compared to other orientations where the maximum difference is 0.24, indicating that the partial dislocations can experience the largest difference in shear stress, leading to the extension of SFs.

Fig. 5 presents the stacking fault probability analysis results for CCN and CCN—N. Stacking fault probability  $P_{sf}$  can be measured from the asymmetric evolution of lattice strains in 111 and 222 planes using the following equation [45,46]:

$$P_{sf} = \frac{32\pi}{3\sqrt{3}} [\varepsilon_{222} - \varepsilon_{111}]$$

where  $\varepsilon_{222}$  and  $\varepsilon_{111}$  represents the lattice strains of the 222 and 111 planes, respectively. The evolution of lattice strains and the calculated  $P_{sf}$  for both longitudinal and transverse directions are present in Fig. 5. The averaged  $P_{sf}$  values in CCN and CCN—N are present in Fig. 5c. The increasing rate of  $P_{sf}$  is  $(0.43\pm0.01)\times10^{-3}/\text{strain}\%$  for CCN and (0.51)

 $\pm 0.01) \times 10^{-3}$ /strain% for CCN—N. This implies that, although the SFs in CCN—N exhibit more discrete features, the stacking fault probability in CCN and CCN—N are comparable with each other (i.e.  $\sim\!20\%$  higher in CCN—N).

The higher stacking fault probability in CCN—N compared to CCN implies that CCN—N has a higher fraction of uncorrelated stacking faults, as the stacking fault probability measured using the present method is a representation of the deviation from the periodic close packed structure [47]. Once the SFs are accumulated and consumed to form larger structures such as twin or hcp phase (i.e., correlated SF), they may not affect the lattice asymmetry and be considered in this stacking fault probability calculations. The consumption of SFs to form hcp phase and the resultant reduction in  $P_{sf}$  was also reported in Ref [48].

Microstructure observations at 25% engineering strain reveal the presence of DIPT, resulting in the formation of a blocky *hcp* phase in both samples (Fig. 6). Interestingly, the area fraction of the *hcp* phase is smaller in CCN—N (18%) compared to CCN (31%). With its limited spatial resolution, the EBSD analysis only captures the block *hcp* phase and does not include nanoscale *hcp* phase fractions. Thus, *in situ* synchrotron-based HEXRD is employed to complement the foregoing

observation by EBSD. Fig. 4b presents the *hcp* phase fraction during tensile deformation as measured by HEXRD. The HEXRD results support the EBSD observation that the *hcp* fraction in CCN is more than 10% higher than that in CCN—N at strain levels higher than 5%. Further, the results show that over 30% of the deformation-induced *hcp* grains are nanoscale thin-film, as deduced from the difference between EBSD and HEXRD measurements.

Additional information is recognized from the EBSD phase maps in Fig. 6a that the *hcp* grains exhibit different growth behavior in the samples. Fig. 7a shows histograms of the aspect ratio of the hcp grains having a size of  $0.5–5~\mu m$  in CCN (15% engineering strain) and CCN—N (25% engineering strain). Interestingly CCN exhibits a higher proportion of *hcp* grains with low aspect ratios (<0.2) in CCN (Fig. 7b). An example is given in Fig. 7b for CCN, where blocky *hcp* grains are thin and elongated, extending from one end to the other side of the parent *fcc* grains. In CCN—N (Fig. 7c), thin and elongated *hcp* grains are also observed, but some *hcp* grains also nucleate at grain boundaries and frequently cease growth in the middle of the parent *fcc* grains.

The deformation-induced  $fcc\rightarrow hcp$  transformation has been well documented in the literature [8,49]. The formation of hcp nuclei results from the splitting and reaction of two perfect dislocations, forming six hcp layers with three SFs on every other {111} plane. These nuclei grow through the extension of SFs and combine with other nuclei to reach a macroscopically observable size [49]. Fig. 8 summarizes the microstructural evolution observed in the present samples in Figs. 2–7. In CCN, extended SFs are readily formed, and the embryo of the hcp lamella would be long and continuous, resulting in the continuous SF/nano-hcp pattern. On the other hand, in some grains of CCN-N, the extension of SFs is stopped in the middle of the grains, resulting in the discrete SF/nano-hcp pattern, which can lower the probability of the accumulation of SFs for the development of the bulky hcp lamella. Therefore, hcp martensite more commonly nucleates at grain boundaries where the stress and number density of SFs are high enough for the nucleation. The formation of the discrete and short SFs thus plays a role in the lower amount of deformation-induced hcp martensite in CCN—N.

## 4. Discussion

The present study examines the influence of N on the tensile properties and microstructural response of Co-rich CoCrNi CCA. The CoCrNi sample with N (CCN—N) shows improved tensile properties compared to the N-free sample (CCN). The strain hardening rate of CCN—N is higher at <0.1 strain and >0.3 strain than that of CCN. The significantly different microstructural response of CCN—N is observed upon deformation: the formation of discrete SF and the resultant discrete nano-hcp in ~30% grains at low deformation levels (~5%) and the suppressed DIPT to the hcp phase at higher deformation levels. In this section, we will discuss the different strain hardening behaviors of the samples, the stacking fault energy of CCN, and the fundamental origin of the different

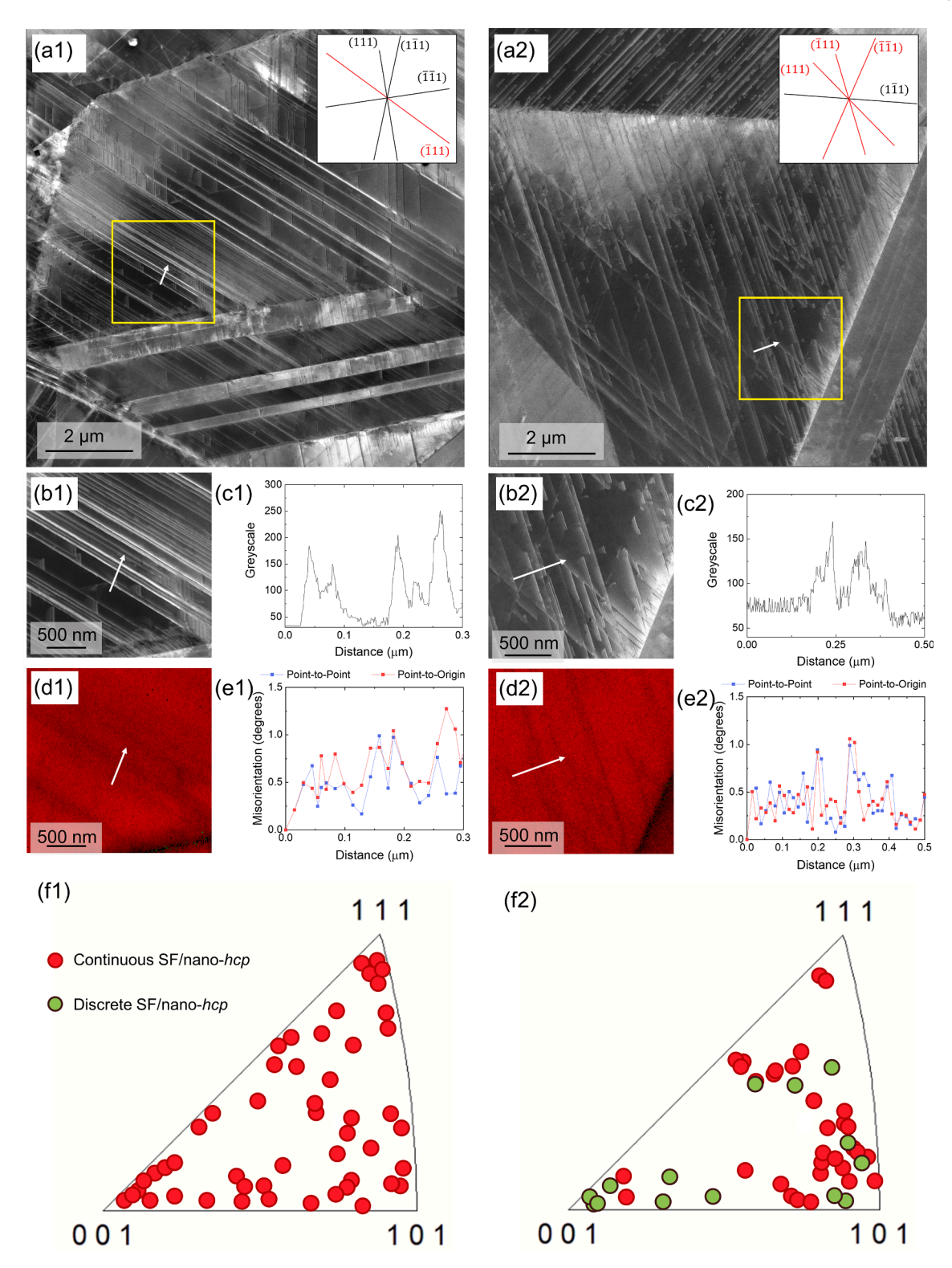


Fig. 4. Deformation substructure of CCN and CCN—N deformed to 5% strain observed by ECCI. (a1) and (a2) Examples of ECCI results; CCN: Continuous SF/nano-hcp distribution; CCN—N: Discrete SF/nano-hcp distribution. (b1) and (b2) Magnified images of the regions marked by the yellow boxes in (a). (c1) and (c2) Greyscale curves measured along the white lines in (b), revealing the fade out of the contrast. (d1) and (d2) Magnified phase maps of the regions marked by the yellow boxes in (a) with the step size of 15 nm. (e1) and (e2) Misorientation line profiles along the white lines in (d2), revealing the absence of characteristic angles for twinning or blocky hcp phase. (f1) and (f2) Different SF/nano-hcp distributions summarized in IPF maps along the normal direction; ~50 grains with different orientations are analyzed in each sample; Red and green dots correspond to continuous SF/nano-hcp and discrete SF/nano-hcp, respectively.

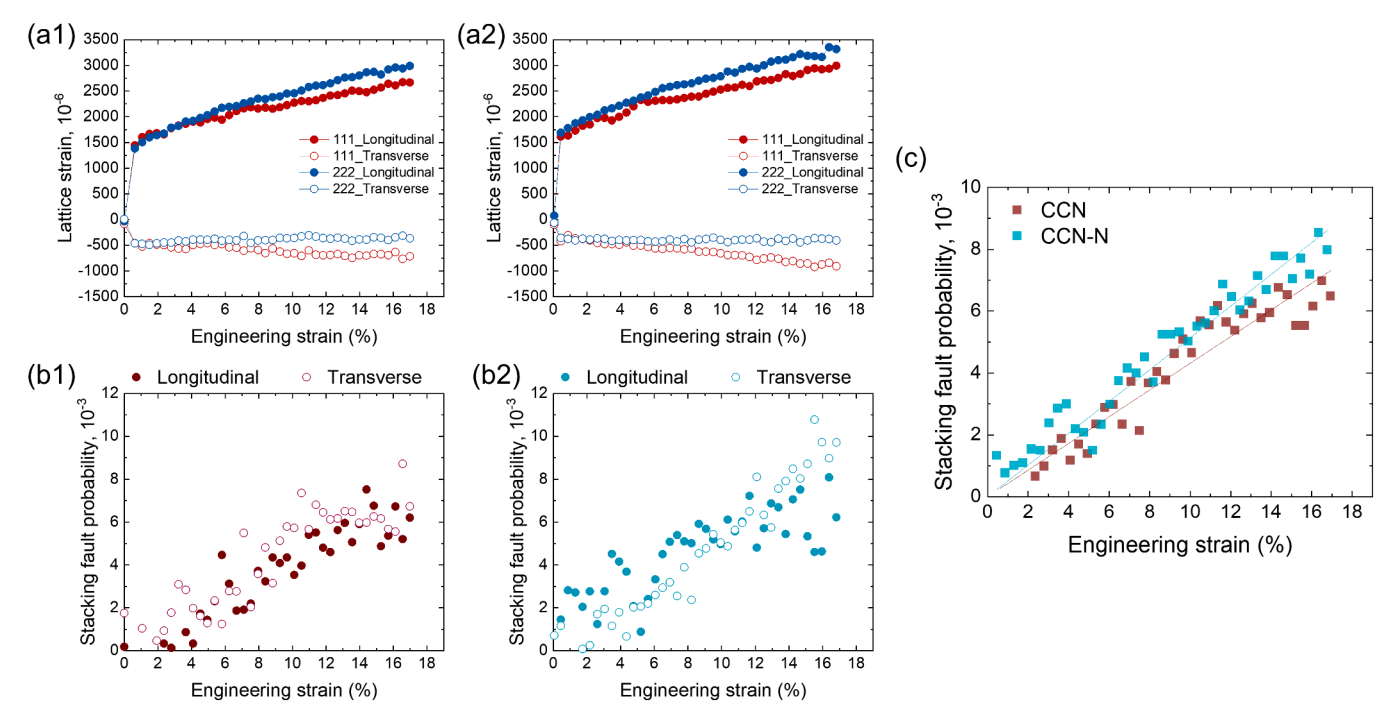
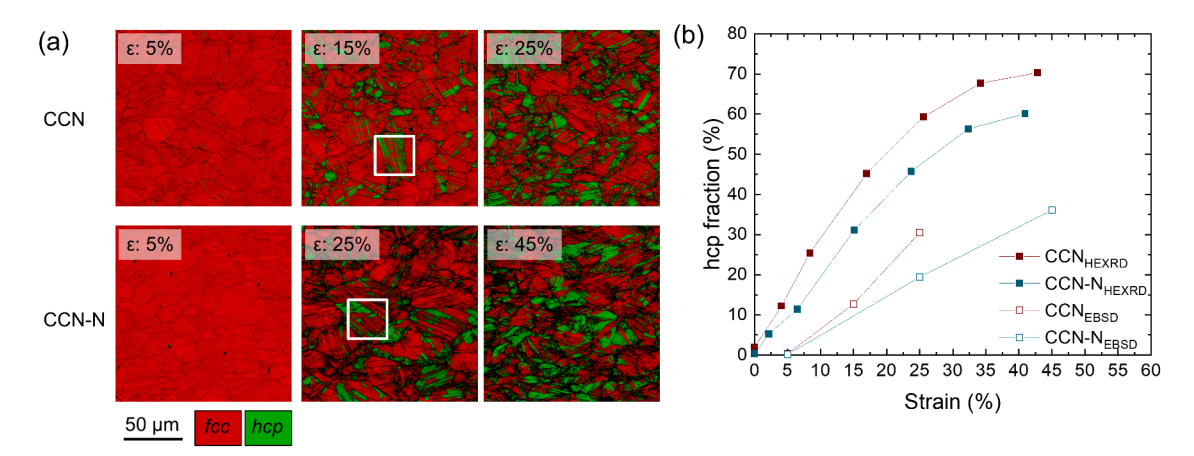


Fig. 5. Stacking fault probability analysis for CCN and CCN—N. (a) Evolution of the lattice strain in the 111 and 222 peaks during deformation of (a1) CCN, (a2) CCN—N. (b) Longitudinal and transverse stacking fault probabilities in (b1) CCN, (b2) CCN—N. (c) Averaged stacking fault probability.



**Fig. 6.** Deformation-induced phase transformation during tensile loading. (a) postmortem EBSD phase maps acquired at different global strain levels with a step size of 90 nm. (b) Phase fraction measured by the *in situ* synchrotron HEXRD diffractograms; the EBSD results are also shown in the chart.

TRIP behavior of CCN—N (i.e., higher contribution and discrete features of SFs in CCN—N).

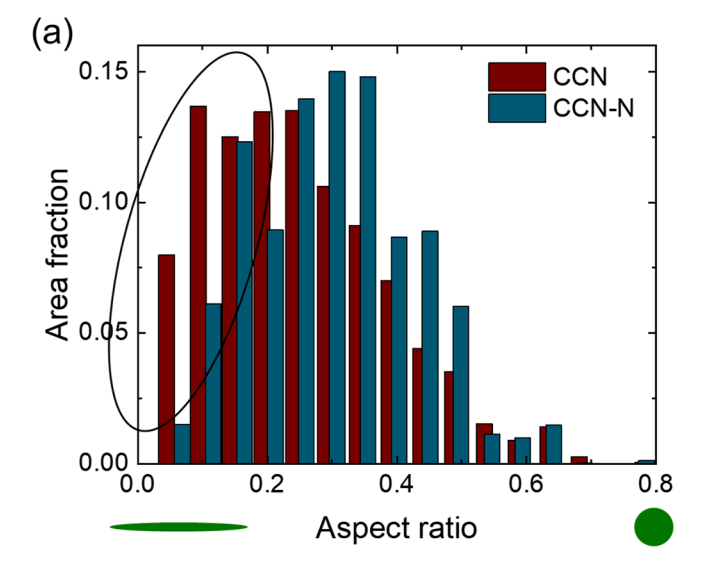
# 4.1. Different strain hardening in model alloys

The strain hardening rate of CCN—N exceeds that of CCN at low strain levels below 10% (Fig. 3b), a regime where the plastic deformation is dominated by SFs and nano-hcp phase (Fig. 4). Recent studies into Co-rich or Cu-rich CCAs have suggested that promotion of SFs and suppression of bulky hcp phase can lead to high strain hardening of the alloys due to multiple factors, including the suppressed dynamic recovery stemming from low or negative intrinsic SFE [9,50], repulsive interaction between SFs, and active Lomer-Cottrell lock formation [9,12, 50,51]. In this study, both CCN and CCN—N have negative  $\gamma_{iSFE}$ , implying a potential for suppressed dynamic recovery. Furthermore, considering that the strain level is low, we anticipate that the higher strain hardening rate of CCN—N compared to CCN is attributable to

factors other than dynamic recovery.

One factor can be the higher SF probability in CCN—N compared to CCN (Fig. 5). SFs in CCN—N are less consumed to form relatively larger structures such as twins or *hcp*-martensite, remaining as uncorrelated monolayer SFs compared to CCN. This higher probability of SFs implies a higher number density of partial dislocations, contributing to high strain hardenability, when considered within the Kocks-Mecking-Estrin model of flow stress  $(\sigma = M\alpha\mu b\sqrt{\rho}(\dot{\epsilon}/\dot{\epsilon}_0)^{1/m})$ , where M is the Taylor factor,  $\alpha$  a constant,  $\mu$  a shear modulus, b is the burgers vector,  $\dot{\epsilon}$  is the strain rate,  $\rho$  is the dislocation density) [52,53].

Moreover, the discrete SF/nano-*hcp* pattern and the lower fraction of *hcp* martensite in CCN—N imply a higher interface fraction that could impede the glide of SFs, enhancing strain hardenability. A micromechanics study demonstrated that the strength of deformation-induced *hcp* martensite in CrMnFeCoNi CCA is almost identical to the *fcc* phase [54]. Therefore, the main contribution of *hcp* martensite to hardening is its provision of boundaries that impede the glide of SFs when it



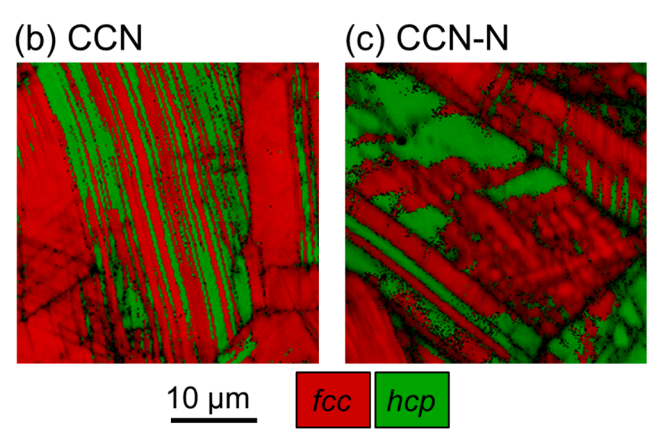


**Fig. 7.** Aspect ratio analysis of the *hcp* grains in CCN and CCN—N. (a) and (b) Magnified images of the regions marked by the white boxes in Fig. 5a, revealing different growth behavior. (c) Aspect ratio histograms calculated considering the *hcp* grains having a size of 0.5–5 μm in Fig. 5a.

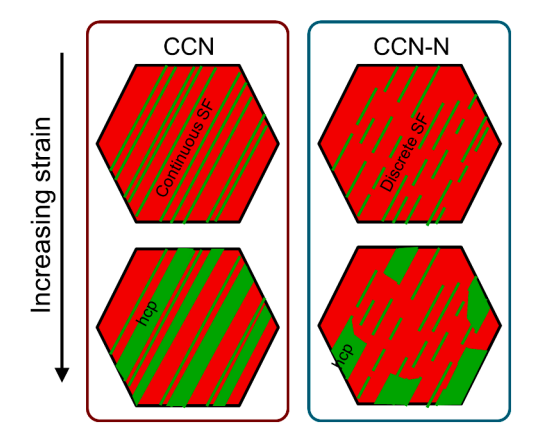


**Fig. 8.** Schematic diagram describing the microstructure evolution with straining in CCN and CCN—N.

intersects with SFs in other directions. In CCN—N, the increased interface fraction from finer nano-hcp can enhance the propensity of interactions between SFs in different directions. Further, although the monolayer SFs are thinner and perceived to be weaker than the bulky structures, effective impingement of SFs can be achieved. This occurs

because when an SF encounters another SF, a Lomer-Cottrell Lock can form at the intersection, resulting in sessile dislocations. For the activation of further glide or cross-slip of the SF (e.g., the formation of extrinsic SFs, twins, or annihilation), it is required to integrate the gliding SF into the perfect lattice dislocation, which is difficult in alloys with a low/negative SFE. As a result, uncorrelated monolayer SFs can effectively interact with other SFs, hindering their motions and increasing strain hardenability.

At strain levels between 10%–30%, the SFs are accumulated and they form *hcp* martensite in both CCN and CCN—N. Although the martensite morphologies show differences (Fig. 7), the rates of martensite formation (Fig. 6b) and the resultant strain hardening rates are similar. At higher strain levels above 30%, the fractions of *hcp* martensite in both alloys reach saturation. The strain hardening rate of CCN rapidly decreases, compared to that of CCN—N. We speculate that in CCN, a higher fraction of brittle *hcp* martensite might facilitate the formation and growth of voids, which may play a role.

Therefore, it can be suggested that promoting SFs while suppressing DIPT not only offers resistance to damage but also results in higher strain hardenability. This effect would be most pronounced for CCAs that exhibit faulting plasticity.

#### 4.2. Negative intrinsic stacking fault energy of CCN

In order to discuss the plasticity mechanism, a thermodynamic assessment is performed to calculate  $\gamma_{iSFE}$  of CCN using a modified Olson and Cohen approach [8,18]. The thermodynamic interaction parameters for CoCrNiW alloy [12] are utilized in the calculation. The interfacial energy and temperature are assumed to be 8 mJ/m² and 300 K, considering a fully coherent structure. Other procedures for the calculation are described in detail in references [12,55]. The full results can be found in Table S2 in Supplementary Materials. Fig. 9a shows the thermodynamically calculated  $\gamma_{iSFE}$  of the ternary Co<sub>x</sub>Cr<sub>33.3</sub>Ni<sub>100-x</sub> CCAs (36<x<46) as a function of Co content. The  $\gamma_{iSFE}$  decreases with increasing the Co content and becomes negative for Co content larger than 27.5%, reaching -44 mJ/m² for the present CCN.

The  $\gamma_{iSFE}$  of the equiatomic CoCrNi is calculated to be -18 mJ/m<sup>2</sup>. This value falls within the range of previously reported values (-51 - 5)mJ/m<sup>2</sup>) obtained using DFT calculations (see the summary of the DFT calculation results of the equiatomic CoCrNi in Ref [56]). This value is supported by previous experiments that demonstrated the transformation from fcc to hcp transformation in this alloy under high pressure and after pressure release [57], thus indicating that the *hcp* phase is energetically more stable than the fcc phase in this alloy. However, these values contrast with the experimentally measured  $\gamma_{\rm iSFE}$  values (8–22 mJ/m<sup>2</sup>) determined using TEM [56]. This discrepancy between the DFT calculated  $\gamma_{\mathit{iSFE}}$  and experimentally measured  $\gamma_{\mathit{iSFE}}$  has been addressed in previous studies, specifically in Ref [18,56]. Intrinsic SFEs have been determined through theoretical calculations [18,58,59] or experiments [60,61]. For experimental determination, SF densities are measured using techniques such as neutron or X-ray diffraction [61,62]; and partial separation [63,64] or dislocation node radius [60,61] are measured by TEM. These methods are based on the classical force balance model (Volterra model) between the repulsive elastic force between partials and the attractive force from positive SFE (as described in Eq. 10.14 in Ref [65]). However, the model breaks down in metals with negative intrinsic SFEs [12,56], as the intrinsic SFE results in repulsion rather than attraction. In this case, both the elastic force between partials and the intrinsic SFE contribute to the extension of stacking faults, potentially leading to the formation of hcp martensite before deformation. This breakdown of the model can be recognized by the fact that the sign of the SF width becomes negative when  $\gamma_{\mathit{iSFE}}$  is negative in the equation. On the one hand, a high Peierls barrier can hinder the extension of SFs, establishing a new force balance in alloys with negative intrinsic SFEs. While this effect might be minor in dilute alloys and has been disregarded in the classical Volterra model for experimental

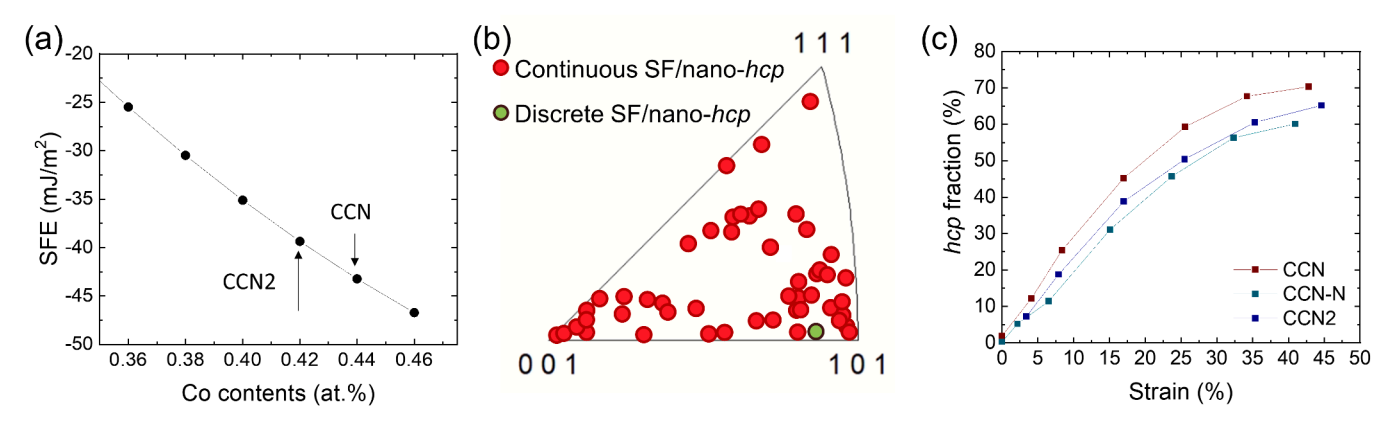


**Fig. 9.** CCN2 having higher  $\gamma_{iSFE}$  than CCN without N. (a) Estimated  $\gamma_{iSFE}$  as a function of Co contents. (b) Summary of deformation substructures at 5% strain; most grains exhibit continuous SF/nano-hcp. (c) Phase fraction measured by the synchrotron HEXRD diffractograms.

measurement of SFEs, it becomes notable in CCAs. Factors such as high solid-solution strengthening (e.g., increasing unstable SFE [18]), short-range ordering, and clustering can amplify lattice shear resistance, thereby increasing the kinetic barrier to the extension of SFs. Therefore, in the presence of high lattice shear resistance, it is feasible for fcc structures to exist in alloys with negative  $\gamma_{iSFE}$ .

Reverting to the current CCN sample, it has higher fraction of Cobalt than the equiatomic CoCrNi alloy, and thus its calculated  $\gamma_{\rm iSFE}$  value is  $\sim\!25~{\rm mJ/m^2}$  lower than that of the equiatomic CoCrNi alloy. Therefore, it can be inferred that the current CCN sample possesses a negative  $\gamma_{\rm iSFE}$ . As a result, the formation of SFs, rather than perfect dislocations or twins with a perfect *fcc* stacking sequence, is energetically favored in the present samples.

## 4.3. Origin of the discrete stacking fault formation in CCN-N

The extension of SFs in alloys depends on the interplay between  $\gamma_{iSFE}$ , which provides a driving force for the extension or shrinkage of SFs; and friction stress, which can suppress the extension of SFs [12,18]. Four approaches are conceivable for explaining the effects of N on the formation of discrete SFs: 1) increased  $\gamma_{iSFE}$ , which can decrease the driving force for the extension of SFs, 2) promotion of SRO, which can lead to the changes in SFEs or friction stress to partial dislocations, 3) segregation at SFs (i.e. Suzuki segregation), which can affect local SFEs in the faulted regions, and 4) increased lattice resistance to the motion of partial dislocations, which can act as pinning sites. This section will discuss the four mechanisms in detail, supported by experimental evidence. Potential other microstructural factors are also discussed.

# 4.3.1. Effects of nitrogen on intrinsic stacking fault energy

The first question is whether the formation of the discrete SFs in CCN—N originates from the increased  $\gamma_{\rm iSFE}$  by N. For CCN—N, to the best of the authors' knowledge, thermodynamic interaction parameters for N are not currently available. An ab-initio calculation demonstrated that N increases the SFE by  $\sim 20$  mJ/m² per 1 at.% [66]¹ in equiatomic CrCoNi. This value (4 mJ/m² per 0.2 at.% N) was used as a first approximation to discuss the effect of  $\gamma_{\rm iSFE}$  in CCN—N. Although the exact value remains unknown, it is expected to represent the potentially maximum increase of  $\gamma_{\rm iSFE}$  by nitrogen. This is because N is known to increase the  $\gamma_{\rm iSFE}$  of other fcc alloys such as Fe-Ni-Cr [19], Fe-Mn-Cr [67], and CrMnFeCoNi [59] by less than 2 mJ/m² per 0.2 at.% N.

A new Co-33.3Cr-24.3Ni (at.%) sample (CCN2), which has a  $\gamma_{iSFE}$  of  $-40 \text{ mJ/m}^2$ , 4 mJ/m<sup>2</sup> higher than CCN, was fabricated and subjected to further investigation. As shown in Fig. 9c, the *in situ* HEXRD results show

that CCN2 has a lower hcp fraction compared to CCN, suggesting that the increased  $\gamma_{iSFE}$  effectively suppresses the martensitic transformation. However, at 5% strain, most SF/nano-hcp features are continuous rather than discrete, similar to CCN (Fig. 9b). This result suggests that while the increase in  $\gamma_{iSFE}$  may reduce the driving force of DIPT, it cannot solely explain the formation of discrete SFs and the suppression of DIPT in CCN—N. This is understandable, since the force balance is now dominated by lattice friction, and changing the SFE does not affect the friction stress [68]. Consequently, in CCN—N, the influence of changes in intrinsic SFE from nitrogen on the formation of discrete SFs is likely to be minimal.

## 4.3.2. Effects of nitrogen on short-range ordering

Studies have suggested that the formation of SROs can stabilize the parent phase by elevating anti-phase boundary energy or influencing Gibbs free energy in various alloys, including NiTi [69,70] and CrCoNi [2,71]. Furthermore, the diffuse antiphase boundary energy of SROs can hinder the thickening of stacking faults [72]. N can form clusters with Cr in austenitic stainless steels [20,73–75] and CoCrMoNi alloys [11] due to their strong chemical interaction [76]. Thus, the addition of N may enhance the SRO, resulting in an increase of SFE and potentially affecting the formation of discrete SFs.

The results obtained from the APT analysis in Fig. 2 reveal the absence of Cr-N precipitates in the resolution limit of APT, despite Cr and N tending to evaporate together, implying the potential for preferential bonding between them. Therefore, we here focus on the impact of nitrogen on the formation of substitutional SRO. Atomic resolution STEM imaging is performed to determine the spatial distribution of substitutional SRO in CCN and CCN—N. Fig. 10a shows the process for determining areas of statistically significant SRO based on atom column intensity comparison and spatial autocorrelation [27,29]. Importantly, L1<sub>2</sub>-type SRO is present based on the alternating atom column intensities of (002) planes in the [110]-oriented images. This pattern is further highlighted by applying a correlation template matching that of the L12 order, giving a correlated intensity where higher values represent high local order. The statistical significance of this correlated intensity is evaluated at each atom column (i) using a local test of spatial autocorrelation, the local Getis-Ord statistic, Gi\*, given by

$$G_i^*(d) = \frac{\sum_{j=1}^{n} w_{ij}(d) x_j - W_i^* \overline{x}}{s \left(\frac{n \sum_{j=1}^{n} \left(w_{ij}^2\right) - W_i^{*2}}{n-1}\right)^{\frac{1}{2}}}$$

where

$$W_i^* = \sum_{i=1}^n w_{ij}(d)$$

 $<sup>^{\</sup>rm 1}$  The value was obtained by averaging the increments of SFEs in all configurations.

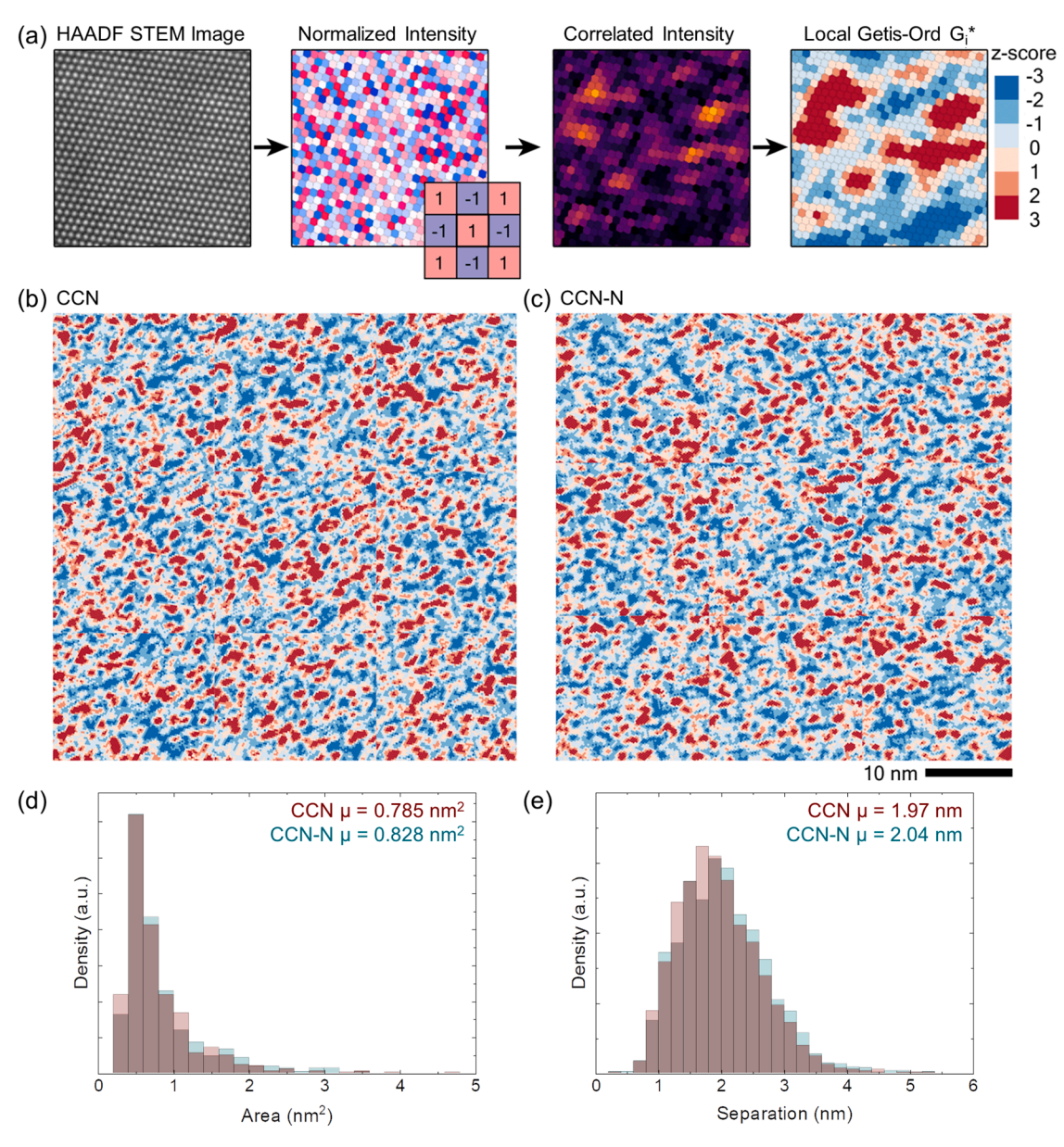


Fig. 10. (a) Overview of calculation of short-range ordered regions from HAADF STEM images, seen in the [110]-oriented images. A correlation template is used to highlight areas of  $L1_2$  order from the normalized intensity, and the local Getis-Ord statistics is used to determine the ordered and disordered hotspots. Nine adjacent images of the resulting order maps from (b) CCN and (c) CCN—N are used to visualize SRO. Statistically significant SRO (d) area and (e) separation distance histograms calculated across individual STEM images, showing no significant changes in substitutional SRO.

$$\overline{x} = \frac{\sum_{j=1}^{n} x_j}{n}$$

$$s = \left(\frac{\sum_{j=1}^{n} x_j^2}{n} - (\overline{x})^2\right)^{\frac{1}{2}}$$

 $w_{ij}$  defines the weights given to neighboring (j) values determined by proximity and number of neighbors, x is the measured feature, and s is the square root of the variance of x. The Gi\* statistic measures local hotspots of order and disorder that are above and below the expected local mean. The local neighbors are taken to be the first and second nearest neighbor atom columns, with the obtained values adjusted for multiple hypothesis testing and representing a z-score/p significance value with respect to the null hypothesis of no local clustering (ordering) [77,78]. For a detailed description of spatial autocorrelation for identifying and correlating local order, see reference [29]. The resulting maps across nine separate imaged regions for CCN and CCN—N

(Figs. 10b and c) show the prevalence of significant atom column ordering (<0.05) (i.e., SRO) given by a dark red color. Interestingly, the size and distribution of the red islands in the two maps are visually akin to each other. For more detailed inspection, the area (i.e., size of SRO) and separation distance (i.e., inter SRO spacing) are measured across these ordered clusters. The resulting histograms between the two alloys (Fig. 10d and e) show no significant change in the spatial distribution of substitutional SRO, indicating a limited impact of N on the formation of substitutional SRO.

Fig. 11 shows the SPD analysis results performed using APT data in Fig. 2d. The results reveal no significant difference between the modulation of Cr-N, Co-N, and Ni-N pairs. This suggests that, although the possibility of preferential bonding between N and Cr exists, the effect might be weak. The solubility of nitrogen in the equiatomic *fcc* CrCoNi CCA is proven to be larger than 0.5 at.% [79], which should be similar to the present samples, considering the fact that the present alloy has the same Cr content. The concentration of N in CCN—N is only 0.2 at.%.

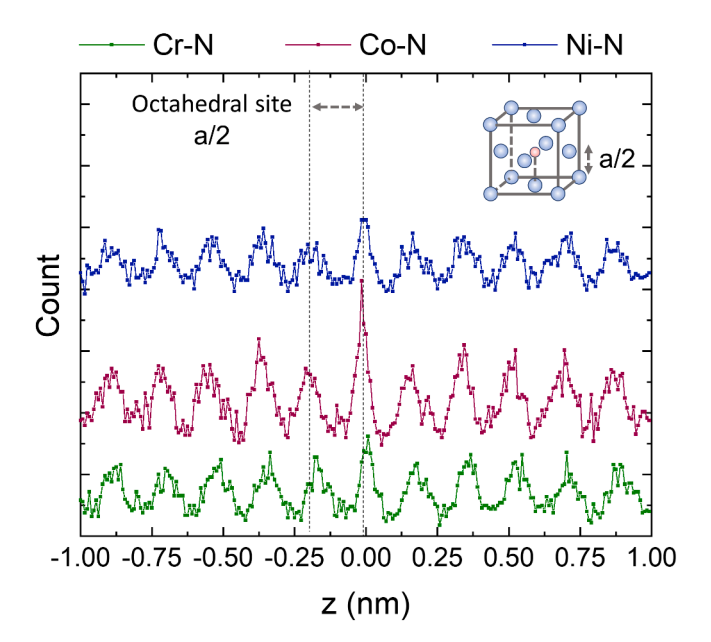


**Fig. 11.** Spatial distribution maps of Cr-N, Co-N, and Ni-N pairs of the pole in undeformed CCN—N (Fig. 2d).

Therefore, the current composition is far away from the phase boundary associated with precipitates of N and other elements, suggesting that the tendency of forming N—Cr SRO may be weak.

## 4.3.3. Segregation of nitrogen at stacking faults

The first two questions discussed concerning the  $\gamma_{iSFE}$  of the alloy matrix are from a global perspective, in which the fluctuation of local

chemistry is presumed to be subtle. In actual alloys, however, the  $\gamma_{\rm ISFE}$  can vary locally, driven by the elemental segregation at the SFs [21,22]. The so-called Suzuki segregation effect has been well documented in concentrated alloy systems such as Cu-Zn [21] and Co-Ni alloys [22,80]. In these alloys, segregation occurs at high temperatures, changing  $\gamma_{\rm ISFE}$  and affecting the extension of SFs. If N segregates at SFs in the present alloys due to its high mobility even at ambient temperature, shrinkage of the SFs can be anticipated as a result of the increase of local SFE.

We thus investigate the elemental segregation at SFs in the deformed CCN-N sample at ~32% strain using APT measurements. Fig. 12a presents the event histogram and 2D contour plot of Co. The analysis is done in the central region (white square), away from the crystallographic pole and zone lines. Fig. 12b presents a 2D density plot of all elements, revealing the presence of diagonal bands with different densities. The bands are not present in the undeformed sample and have a planar shape (see Fig. S4 for a visual representation of the density maps of CCN-N in undeformed and deformed states). The voltage history of the sample (Fig. S5), particularly the voltage at the ion sequence number between 3.5e7-6e7 (where the analyzed region in Fig. 12 belongs to), is smooth and without sudden disruptions, implying that the planar feature is not a result of small fractures in the sample. Given that the alloy deforms solely through the formation of SFs or their accumulations, the only structural features in CCN-N that could constitute these bands are SFs or their accumulated hcp martensite. The distance between SFs, d, can be calculated using  $d = d_{111}/P_{sf}$ , where  $d_{111}$  is the Dspacing of 111 planes. As estimated from Fig. 5c, the expected distance between SFs should be around 6-7 nm, which is shorter than the distances between the planar bands (10-30 nm) in Fig. 12b. This discrepancy might arise from the accumulation of SFs at high strain levels, which is supported by the presence of hcp martensite in the APT tip (Fig. S4).

The 2D concentration maps in Fig. 12b reveal that N, despite its

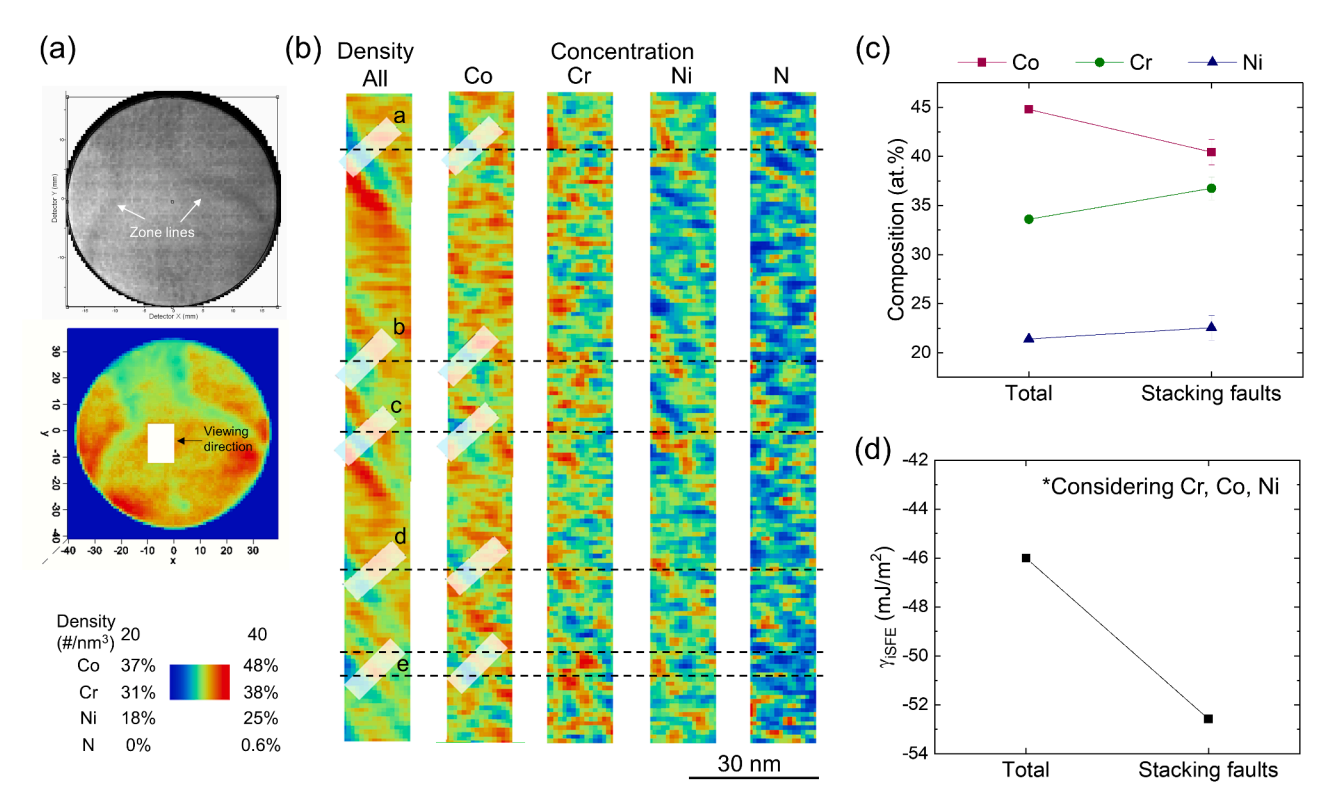


Fig. 12. APT measured elemental distribution in CCN—N after 32% deformation, capturing SFs. (a) Event histogram and 2-D contour plot of Co displaying crystallographic pole and zone lines. (b) 2-dimensional density (all elements) and concentration (Co, Cr, Ni, CrN) plots. Diagonal features are seen, which are SFs. (c) Comparison between the total composition (Table 1) and average composition at stacking faults, obtained by analyzing the five 1-D concentration profiles along the white box in (b), showing the depletion of Co and enrichment of Ni or Cr in SFs; See Fig. S6 for the detailed procedure. (d) Estimated  $\gamma_{iSFE}$  considering Cr, Co, and Ni in the SFs and the total composition.

interstitial nature, does not have a strong correlation with the SFs. Therefore, the segregation of N is unlikely to have a significant impact on the  $\gamma_{iSFE}$  of the SFs. Surprisingly, substitutional Co, Cr, and Ni show different concentrations in the SFs, with Co being depleted and Cr and Ni enriched (Fig. 12b, c; See Fig. S6 for individual 1-D concentration profile). The cause of this segregation is yet to be fully understood, as substitutional elements are expected to have slow diffusivity at room temperature. A previous TEM-EDS measurement also reported the segregation of substitutional elements at SFs in a CrMnFeCoNi CCA [51]. The segregation could have occurred during deformation, or the diffusion kinetics could have been enhanced due to the small curvature radius of the APT tip (for example, driven by the Young-Laplace pressure). Local  $\gamma_{iSFE}$  at SFs is calculated and plotted in Fig. 12d considering the concentration of substitutional elements. Despite the lower Co composition, the estimated  $\gamma_{iSFE}$  is -53 mJ/m<sup>2</sup>, lower than  $\gamma_{iSFE}$  (-46 $mJ/m^2$ ) considering the total composition of the sample. This is due to the higher concentration of Cr, which has a stronger impact than Co in reducing  $\gamma_{iSFE}$ . This trend of lower  $\gamma_{iSFE}$  at SFs aligns with previous studies, where the segregation of elements to SFs occurred to further decrease the SFE and stabilize SFs [81]. Lower  $\gamma_{iSFE}$  implies the extension of SFs. Therefore, Consequently, irrespective of whether the segregation occurred during deformation or emerged as post-preparation artifacts of the APT tips, the SFE change due to the elemental segregation cannot explain the formation of discrete SFs (and nano-hcp as well) in CCN-N.

## 4.3.4. Effects of nitrogen on pinning partial dislocations

The extension of SFs can also be affected by their mechanical interaction with solute elements, which can act as pinning sites for partial dislocations [17]. This effect is evident in the fact that CCN-N has a yield strength similar to CCN (Fig. 3a), despite having a larger grain size (Fig. 1). To understand the pinning effect better, the activation volume of dislocations in CCN, CCN-N, and CCN2 is measured via repeated stress-relaxation tests [34,82] (See Method 2.3.2 for the experimental procedure). Fig. 13a and the inset show the stress-strain and relaxation curves of CCN—N during the test, respectively. By fitting the relaxation curves (stress vs. time), one can obtain the physical activation volume, which represents the volume of matter that is swept by the thermally activated dislocation segments without hindrance from obstacles. The detailed fitting procedures can be found in Refs. [34]. The measured physical activation volume V is shown in Fig. 13b. Interestingly, CCN and CCN2 have similar activation volumes of ~150b3 (2.3 nm3), where b is the Burgers vector at  $\sim$ 1% true strain, indicating that the activation volume is insensitive to the global  $\gamma_{iSFE}$ . On the other hand, CCN—N has  $\sim$ 25% smaller activation volume ( $\sim$ 110b<sup>3</sup>; 1.7 nm<sup>3</sup>).

The activation volume is linked to the average distance between the effective obstacles hindering the dislocation motion [32]. For instance, a molecular dynamics study [72] showed that the activation volume in the

equiatomic *fcc* CrCoNi CCA increases with the increasing distance between SROs. Assuming that dislocation segments are pinned by shearable spherical obstacles with a small volume fraction (i.e., average distance between obstacles l>> average radius of obstacles r), the activation area (V/b) becomes on average equal to  $l^2$ . Based on this assumption, the activation volume of each sample gives the average effective obstacle distances (i.e., l) of 3 nm for CCN ( $l_{CCN}$ ) and CCN2 and 2.6 nm for CCN—N ( $l_{CCN-N}$ ).

In the present samples, the obstacles at 1% strain can primarily be SROs and interstitial atoms. For CCN, the average separation distance between SROs is  $\sim$ 2 nm, which is shorter than  $l_{CCN}$ , suggesting that not every single substitutional SRO island is an effective obstacle to mobile dislocations. For CCN—N, the shorter  $l_{CCN-N}$  compared to  $l_{CCN}$  implies the contribution of additional obstacles beyond the substitutional SROs, which are the N interstitial atoms or small clusters surrounding the N atoms (which are beyond the resolution of APT). The average distance between the N atoms is  $\sim$ 2 nm, considering the N content (0.2 at.%), which is shorter than  $l_{CCN-N}$ , indicating that not every single N atom or cluster can pin the dislocation segments. Therefore, both substitutional SROs and solute N are expected to contribute to the pinning effect together, leading to the shorter l and the smaller V in CCN—N compared to CCN.

# 4.3.5. Potential other microstructural factors on the development of stacking faults and hcp martensite

In addition to the nanoscale structural factors discussed above, the development of SF and hcp martensite may also depend on microstructural factors such as texture and grain size. As presented in Fig. 4f2, grains close to the  $\langle 111 \rangle / ND$  directions in CCN—N display continuous SFs. This is due to the significant Schmid factor difference between partial dislocations, which results in the maximum difference in shear stress between leading and trailing partials, thereby promoting the extension of SFs [44,83]. Consequently, grain orientation can influence the extension of SFs. However, it does not alter the interpretation in this study since both CCN and CCN—N exhibit a random distribution of grain orientations.

Grain size is another potential influential factor. Larger grain sizes favor the formation of hcp martensite, as adequately large martensite can induce high stress at the tip, triggering further transformation in various directions [84]. In this study, CCN—N (~23  $\mu$ m) has a slightly larger grain size than CCN (~19  $\mu$ m). This suggests that the grain size effect should encourage the formation of the hcp phase in CCN—N, even though observations indicate a lower hcp fraction in CCN—N. Therefore, the discrete SFs and lower hcp fraction in CCN—N are unlikely to stem from microstructural factors, although the factors could be generally influential on the TRIP behavior.

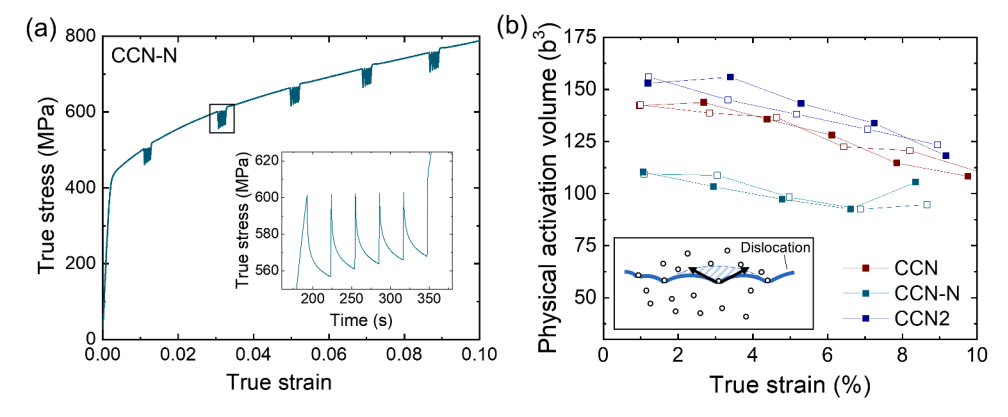


Fig. 13. Repeated load relaxation tests. (a) Exemplary tensile stress-strain curve of CCN—N. The inset shows a set of repeated load relaxation tests (duration 30 s each, five times) at  $\sim$ 0.03 true strain. (b) Physical activation volume of thermally activated dislocation motions in CCN, CCN—N, and CCN2, as a function of the true strain. CCN—N has  $\sim$ 25% smaller activation volume implying a higher density of obstacles.

4.3.6. Summary of the origin of discrete stacking faults in CCN-N and implication to faulting plasticity

To uncover the origin of the formation of discrete SFs in CCN—N, we evaluate four potential effects of N on the extension of SFs: intrinsic SFE, formation of substitutional SRO, segregation and SFE of the SFs, and mechanical pinning of partial dislocations. The first three effects appear to be relatively insignificant, likely due to the diluted nature of N in CCN—N. In contrast, a drastic difference was observed in the mechanical pinning effect. The results suggest that the formation of discrete SFs in CCN—N primarily originates from the mechanical pinning effect of partial dislocations by N (small N clusters beyond the resolution of APT). Therefore, the suppression of DIPT necessitates additional obstacles to hinder the extension of SFs. Indeed, the previously reported CCAs that exhibit faulting plasticity are characterized by strong SRO formation tendencies, such as W in CoCrNiW [12,85] and high concentrations of N and Mo in CoCrMoN [11].

Moreover, considering the fact that nanoscale precipitates can effectively refine the twins in high-manganese TWIP steels [86], obstacles can be any nanoscale heterogeneities, such as SRO, clustering, interstitial elements, chemical fluctuation, and precipitates. The effects of these obstacles on the SF extension and DIPT can differ, depending on their strength, size, separation distance, and (diffuse) antiphase boundary energy. For example, SRO and random chemical ordering can inhibit and promote cross slip of dislocations, respectively [87]. Therefore, further studies are required to understand the impacts of these obstacles on achieving faulting plasticity.

While it is critical to possess low or negative  $\gamma_{iSFE}$  to form SFs, the threshold  $\gamma_{iSFE}$  activating faulting plasticity remains unclear. Considering that the equiatomic CoCrNi CCA exhibiting TWIP has a negative  $\gamma_{iSFE}$ , faulting plasticity may occur only in CCAs with larger negative  $\gamma_{iSFE}$  to prevent twinning. We further propose that lowering the  $\gamma_{iSFE}$  to larger negative values are beneficial to activate faulting plasticity for several reasons. It has been suggested that negative  $\gamma_{iSFE}$  energetically stabilizes the formation of SFs over perfect slip and twin faults [40,41]. Furthermore, if the  $\gamma_{iSFE}$  is not sufficiently low, the SFs can more readily recombine to form perfect dislocations in the presence of applied stress, enabling cross-slip when intersecting with SFs in different directions, leading to the formation of twin, annihilation or thickening of SFs [88]. Therefore, with positive  $\gamma_{iSFE}$ , the emergence of twin or hcp martensite during deformation is highly probable, inducing sequential faulting plasicity, TWIP, and TRIP behavior.

Consequently, we conclude that both a negative  $\gamma_{iSFE}$  and the presence of atomic- and nano-scale obstacles are essential for the faulting plasticity effect to occur, and further research is required to deeply understand their effects on faulting plasticity.

#### 5. Conclusions

We studied the effects of 0.2 at.% N on the stacking fault and transformation-induced plasticity in a Co-rich CoCrNi complex-concentrated alloy with negative intrinsic stacking fault energy using atom-probe tomography, revolving scanning transmission electron microscopy, interrupted electron backscattered diffraction and electron channeling contrast imaging probing, *in situ* high-energy X-ray diffraction during tensile testing, thermodynamic calculation on intrinsic stacking fault energy, and repeated stress relaxation testing methods. The following conclusions can be drawn from the study:

- (1) Atom-probe tomography analysis reveals that the N atoms are dissolved in the matrix without forming detectable precipitates. The spatial distribution analysis does not show a significant difference between Cr-N, Co-N, and Ni-N pairs.
- (2) The presence of dilute N results in different microstructural responses upon deformation, including the formation of discrete stacking faults and nano-hcp phase at early deformation levels and suppressed deformation-induced phase transformation at

- later stages. The formation of the discrete stacking faults is the cause of the suppression of deformation-induced phase transformation.
- (3) Four potential effects of N on stacking faults are evaluated, including intrinsic stacking fault energy, formation of substitutional short-range order, segregation and stacking fault energy of stacking faults, and mechanical pinning of partial dislocations. The formation of discrete stacking faults in the N-containing sample is attributed to the mechanical pinning of partial dislocations by N (or small N clusters beyond the resolution of atom probe tomography).
- (4) These points altogether lead to the conclusion that both a negative intrinsic stacking fault energy and the presence of atomicand nano-scale obstacles are essential for the promotion of faulting plasticity and suppression of deformation-induced phase transformation and transformation-induced plasticity.
- (5) Promoting stacking faults while suppressing deformationinduced martensitic transformation not only offers resistance to damage but also results in higher strain hardenability. This effect would be most pronounced for CCAs that exhibit faulting plasticity.

## **Declaration of Competing Interest**

The authors declare that they have no known competing financial interests or personal relationships that could have appeared to influence the work reported in this paper.

## Acknowledgments

This work was supported by U.S. National Science Foundation (NSF) under the grant DMREF-1922206. *In situ* synchrotron tensile tests were conducted at beamline 11-ID-C of the Advanced Photon Source, which was supported by the U.S. Department of Energy, Office of Science, Office of Basic Energy Sciences, under Contract No. DE-AC02-06CH11357. The authors thank Dr. Robert Ulfig from CAMECA for the discussion on the APT results.

# Supplementary materials

Supplementary material associated with this article can be found, in the online version, at doi:10.1016/j.actamat.2023.119349.

## References

- [1] H.S. Oh, S.J. Kim, K. Odbadrakh, W.H. Ryu, K.N. Yoon, S. Mu, F. Körmann, Y. Ikeda, C.C. Tasan, D. Raabe, T. Egami, E.S. Park, Engineering atomic-level complexity in high-entropy and complex concentrated alloys, Nat Commun. 10 (2019) 1–8, https://doi.org/10.1038/s41467-019-10012-7.
- [2] R. Zhang, S. Zhao, J. Ding, Y. Chong, T. Jia, C. Ophus, M. Asta, R.O. Ritchie, A. M. Minor, Short-range order and its impact on the CrCoNi medium-entropy alloy, Nature (2020) 581, https://doi.org/10.1038/s41586-020-2275-z.
- [3] D. Liu, Q. Yu, S. Kabra, M. Jiang, P. Forna-Kreutzer, R. Zhang, M. Payne, F. Walsh, B. Gludovatz, M. Asta, A.M. Minor, E.P. George, R.O. Ritchie, Exceptional fracture toughness of CrCoNi-based medium-and high-entropy alloys at 20 kelvin, Science 378 (2022) (1979) 978–983.
- [4] S.S. Sohn, A. Kwiatkowski da Silva, Y. Ikeda, F. Körmann, W. Lu, W.S. Choi, B. Gault, D. Ponge, J. Neugebauer, D. Raabe, Ultrastrong medium-entropy singlephase alloys designed via severe lattice distortion, Adv. Mater. 31 (2019) 1–8, https://doi.org/10.1002/adma.201807142.
- [5] Z. Li, K.G. Pradeep, Y. Deng, D. Raabe, C.C. Tasan, Metastable high-entropy dualphase alloys overcome the strength-ductility trade-off, Nature 534 (2016) 227–230, https://doi.org/10.1038/nature17981.
- [6] X. Wu, Z. Li, Z. Rao, Y. Ikeda, B. Dutta, F. Körmann, J. Neugebauer, D. Raabe, Role of magnetic ordering for the design of quinary TWIP-TRIP high entropy alloys, Phys. Rev. Mater. 4 (2020) 1–14, https://doi.org/10.1103/PhysRevMaterials.4.033601.
- [7] B.C. De Cooman, Y. Estrin, S.K. Kim, Twinning-induced plasticity (TWIP) steels, Acta Mater. 142 (2018) 283–362, https://doi.org/10.1016/j.actamat.2017.06.046.
- [8] G.B. Olson, M. Cohen, A general mechanism of martensitic nucleation: part I. General concepts and the FCC HCP transformation, Metall. Trans. A 7A (1976) 1897–1904.

- [9] Y.Z. Tian, L.J. Zhao, S. Chen, A. Shibata, Z.F. Zhang, N. Tsuji, Significant contribution of stacking faults to the strain hardening behavior of Cu-15%Al alloy with different grain sizes. Sci. Rep. 5 (2015). https://doi.org/10.1038/crep16707.
- with different grain sizes, Sci. Rep. 5 (2015), https://doi.org/10.1038/srep16707.

  [10] W. Li, S. Lu, Q.M. Hu, S.K. Kwon, B. Johansson, L. Vitos, Generalized stacking fault energies of alloys, J. Phys. Condens. Matter 26 (2014), https://doi.org/10.1088/0953-8984/26/26/265005.
- [11] K. Yamanaka, M. Mori, A. Chiba, Nanoarchitectured Co-Cr-Mo orthopedic implant alloys: nitrogen-enhanced nanostructural evolution and its effect on phase stability, Acta Biomater. 9 (2013) 6259–6267, https://doi.org/10.1016/j. actbio.2012.12.013.
- [12] S. Wei, C.C. Tasan, Deformation faulting in a metastable CoCrNiW complex concentrated alloy: a case of negative intrinsic stacking fault energy? Acta Mater. 200 (2020) 992–1007, https://doi.org/10.1016/j.actamat.2020.09.056.
- [13] S. Wei, J. Kim, C.C. Tasan, Boundary micro-cracking in metastable Fe45Mn35Co10Cr10 high-entropy alloys, Acta Mater. (2019), https://doi.org/ 10.1016/j.actamat.2019.01.036.
- [14] S. Takaki, T. FURUYA, Y. Tokunaga, Effect of Si and Al additions on the low temperature fracture mode of Fe-27Mn alloys, ISIJ Int. 30 (1990) 632–638.
- [15] Z. Pei, B. Dutta, F. Körmann, M. Chen, Hidden effects of negative stacking fault energies in complex concentrated alloys, Phys. Rev. Lett. 126 (2021), https://doi. org/10.1103/PhysRevLett.126.255502.
- [16] C. Baruffi, M. Ghazisaeidi, D. Rodney, W.A. Curtin, Equilibrium versus non-equilibrium stacking fault widths in NiCoCr, Scr. Mater. 235 (2023), https://doi.org/10.1016/j.scriptamat.2023.115536.
- [17] K. Gan, D. Yan, S. Zhu, Z. Li, Interstitial effects on the incipient plasticity and dislocation behavior of a metastable high-entropy alloy: nanoindentation experiments and statistical modeling, Acta Mater. 206 (2021), https://doi.org/ 10.1016/j.actamat.2021.116633.
- [18] S. Kibey, J.B. Liu, M.J. Curtis, D.D. Johnson, H. Sehitoglu, Effect of nitrogen on generalized stacking fault energy and stacking fault widths in high nitrogen steels, Acta Mater. 54 (2006) 2991–3001, https://doi.org/10.1016/j. actamat 2006 02 048
- [19] J.M. Kim, S.J. Kim, J.H. Kang, Effects of short-range ordering and stacking fault energy on tensile behavior of nitrogen-containing austenitic stainless steels, Mater. Sci. Eng. A 836 (2022), https://doi.org/10.1016/j.msea.2022.142730.
- [20] Y. Xie, G. Miyamoto, T. Furuhara, Nanosized Cr-N clustering in expanded austenite layer of low temperature plasma-nitrided Fe-35Ni-10Cr alloy, Scr. Mater. 213 (2022), https://doi.org/10.1016/j.scriptamat.2022.114637.
- [21] H. Suzuki, Segregation of solute atoms to stacking faults, J. Phys. Soc. Japan 17 (1962) 322–325.
- [22] D. Wen, M.S. Titus, First-principles study of Suzuki segregation at stacking faults in disordered face-centered cubic Co-Ni alloys, Acta Mater. 221 (2021), https://doi. org/10.1016/j.actamat.2021.117358.
- [23] P.J. Yang, Q.J. Li, T. Tsuru, S. Ogata, J.W. Zhang, H.W. Sheng, Z.W. Shan, G. Sha, W.Z. Han, J. Li, E. Ma, Mechanism of hardening and damage initiation in oxygen embrittlement of body-centred-cubic niobium, Acta Mater. 168 (2019) 331–342, https://doi.org/10.1016/j.actamat.2019.02.030.
- [24] L. Lutterotti, S. Matthies, H.-R. Wenk, A.S. Schultz, J.W. Richardson Jr, Combined texture and structure analysis of deformed limestone from time-of-flight neutron diffraction spectra, J. Appl. Phys. 81 (1997) 594–600.
- [25] L. Lutterotti, R. Vasin, H.R. Wenk, Rietveld texture analysis from synchrotron diffraction images. I. Calibration and basic analysis, Powder Diffr. 29 (2014) 76–84, https://doi.org/10.1017/S0885715613001346.
- [26] A.K. Singh, C. Balasingh, H.K. Mao, R.J. Hemley, J. Shu, Analysis of lattice strains measured under nonhydrostatic pressure, J. Appl. Phys. 83 (1998) 7567–7575, https://doi.org/10.1063/1.367872.
- [27] X. Sang, J.M. LeBeau, Revolving scanning transmission electron microscopy: correcting sample drift distortion without prior knowledge, Ultramicroscopy 138 (2014) 28–35, https://doi.org/10.1016/j.ultramic.2013.12.004.
- [28] C. Niu, A.J. Zaddach, A.A. Oni, X. Sang, J.W. Hurt, J.M. Lebeau, C.C. Koch, D. L. Irving, Spin-driven ordering of Cr in the equiatomic high entropy alloy NiFeCrCo, Appl. Phys. Lett. 106 (2015), https://doi.org/10.1063/1.4918996.
- [29] M. Xu, A. Kumar, J.M. LeBeau, Correlating local chemical and structural order using Geographic Information Systems-based spatial statistics, Ultramicroscopy (2022), 113642, https://doi.org/10.1016/j.ultramic.2022.113642.
- [30] R.S. Bivand, D.W.S. Wong, Comparing implementations of global and local indicators of spatial association, Test. 27 (2018) 716–748, https://doi.org/ 10.1007/s11749-018-0599-x.
- [31] M. Tennekes, Tmap: thematic maps in R, J. Stat. Softw. 84 (2018), https://doi.org/ 10.18637/iss.v084.i06.
- [32] A. Argon, Strengthening Mechanisms in Crystal Plasticity, Oxford University Press on Demand, 2008.
- [33] S. Wei, D.P. Moriarty, M. Xu, J.M. LeBeau, C.C. Tasan, On the plastic deformation of a CoCrFeNiW-C alloy at elevated temperatures: part I. Serrated plastic flow and its latent dynamics, Acta Mater. 242 (2023), https://doi.org/10.1016/j. actamat 2022 118430
- [34] G. Laplanche, J. Bonneville, C. Varvenne, W.A. Curtin, E.P. George, Thermal activation parameters of plastic flow reveal deformation mechanisms in the CrMnFeCoNi high-entropy alloy, Acta Mater. (2018), https://doi.org/10.1016/j. actamat.2017.10.014.
- [35] M. Herbig, M. Kuzmina, C. Haase, R.K.W. Marceau, I. Gutierrez-Urrutia, D. Haley, D.A. Molodov, P. Choi, D. Raabe, Grain boundary segregation in Fe-Mn-C twinning-induced plasticity steels studied by correlative electron backscatter diffraction and atom probe tomography, Acta Mater. 83 (2015) 37–47, https://doi. org/10.1016/j.actamat.2014.09.041.

[36] F.F. Dear, P. Kontis, B. Gault, J. Ilavsky, D. Rugg, D. Dye, Mechanisms of Ti3Al precipitation in hcp  $\alpha$ -Ti, Acta Mater. 212 (2021), https://doi.org/10.1016/j. actamat.2021.116811.

- [37] D.R. Kingham, The post-ionization of field evaporated ions: a theoretical explanation of multiple charge states, Surf. Sci. 116 (1982) 273–301.
- [38] S. Zaefferer, N.N. Elhami, Theory and application of electron channelling contrast imaging under controlled diffraction conditions, Acta Mater. 75 (2014) 20–50, https://doi.org/10.1016/j.actamat.2014.04.018.
- [39] S. Wei, G. Zhu, C.C. Tasan, Slip-twinning interdependent activation across phase boundaries: an in-situ investigation of a Ti-Al-V-Fe (α+β) alloy, Acta Mater. 206 (2021), https://doi.org/10.1016/j.actamat.2020.116520.
- [40] X. Li, S. Schönecker, L. Vitos, X. Li, Generalized stacking faults energies of face-centered cubic high-entropy alloys: a first-principles study, Intermetallics (Barking). 145 (2022). https://doi.org/10.1016/j.intermet.2022.107556.
- [41] Z.H. Jin, S.T. Dunham, H. Gleiter, H. Hahn, P. Gumbsch, A universal scaling of planar fault energy barriers in face-centered cubic metals, Scr. Mater. 64 (2011) 605–608, https://doi.org/10.1016/j.scriptamat.2010.11.033.
- [42] S.M. Copley, B.H. Kear, The dependence of the width of a dissociated dislocation on dislocation velocity\*, Acta Metall. 16 (1968) 227–231.
- [43] W.S. Choi, B.C. De Cooman, S. Sandlöbes, D. Raabe, Size and orientation effects in partial dislocation-mediated deformation of twinning-induced plasticity steel micro-pillars, Acta Mater. 98 (2015) 391–404, https://doi.org/10.1016/j. actamat 2015 06 065
- [44] I. Karaman, H. Sehitoglu, K. Gall, Y.I. Chumlyakov, H.J. Maier, Deformation of single crystal hadfield steel by twinning and slip, Acta Mater. 48 (2000) 1945–1959. www.elsevier.com/locate/actamat.
- [45] B.E. Warren, X-ray studies of deformed metals, Progr. Metal Phys. 8 (1959).
- [46] R.P. Reed, R.E. Schramm, Relationship between stacking-fault energy and x-ray measurements of stacking-fault probability and microstrain, J. Appl. Phys. 45 (1974) 4705–4711.
- [47] M.S. Paterson, X-ray diffraction by face-centered cubic crystals with deformation faults, J. Appl. Phys. 23 (1952) 805–811, https://doi.org/10.1063/1.1702312.
- [48] S. Wei, J. Kim, J.L. Cann, R. Gholizadeh, N. Tsuji, C.C. Tasan, Plastic strain-induced sequential martensitic transformation, Scr. Mater. 185 (2020) 36–41, https://doi. org/10.1016/j.scriptamat.2020.03.060.
- [49] S. Mahajan, M.L. Green, D. Brasen, A model for the FCC HCP transformation, its applications, and experimental evidence, Metall. Trans. A 8A (1977) 283–293.
- [50] D. Wei, L. Wang, Y. Zhang, W. Gong, T. Tsuru, I. Lobzenko, J. Jiang, S. Harjo, T. Kawasaki, J.W. Bae, W. Lu, Z. Lu, Y. Hayasaka, T. Kiguchi, N.L. Okamoto, T. Ichitsubo, H.S. Kim, T. Furuhara, E. Ma, H. Kato, Metalloid substitution elevates simultaneously the strength and ductility of face-centered-cubic high-entropy alloys, Acta Mater. 225 (2022), https://doi.org/10.1016/j.actamat.2021.117571.
- [51] S. Chen, H.S. Oh, B. Gludovatz, S.J. Kim, E.S. Park, Z. Zhang, R.O. Ritchie, Q. Yu, Real-time observations of TRIP-induced ultrahigh strain hardening in a dual-phase CrMnFeCoNi high-entropy alloy, Nat. Commun. 11 (2020) 1–8, https://doi.org/ 10.1038/s41467-020-14641-1.
- [52] U.F. Kocks, H. Mecking, Physics and phenomenology of strain hardening: the FCC case, 2003. www.elsevier.com/locate/pmatsci.
- [53] Y. Estrin, H. Mecking, A unified phenomenological description of work hardening and creep based on one-parameter models. Acta Metall. 32 (1984) 57–70.
- [54] W.S. Choi, H.S. Oh, M. Lai, N.V. Malyar, C. Kirchlechner, E.S. Park, P.P. Choi, Effects of transformation-induced plasticity on the small-scale deformation behavior of single crystalline complex concentrated alloys, Scr. Mater. 176 (2020) 122–125, https://doi.org/10.1016/j.scriptamat.2019.09.015.
- [55] S. Curtze, V.T. Kuokkala, A. Oikari, J. Talonen, H. Hänninen, Thermodynamic modeling of the stacking fault energy of austenitic steels, Acta Mater. 59 (2011) 1068–1076, https://doi.org/10.1016/j.actamat.2010.10.037.
- [56] X. Sun, S. Lu, R. Xie, X. An, W. Li, T. Zhang, C. Liang, X. Ding, Y. Wang, H. Zhang, L. Vitos, Can experiment determine the stacking fault energy of metastable alloys? Mater Des. (2021) 199, https://doi.org/10.1016/j.matdes.2020.109396.
- [57] F.X. Zhang, S. Zhao, K. Jin, H. Bei, D. Popov, C. Park, J.C. Neuefeind, W.J. Weber, Y. Zhang, Pressure-induced fcc to hcp phase transition in Ni-based high entropy solid solution alloys, Appl. Phys. Lett. 110 (2017), https://doi.org/10.1063/ 1.1073627
- [58] G. Chai, R. Siriki, J. Nordström, Z. Dong, L. Vitos, Roles of nitrogen on TWIP in advanced austenitic stainless steels, Steel Res. Int. (2022), https://doi.org/ 10.1002/srin.202200359.
- [59] Y. Ikeda, F. Körmann, Impact of N on the stacking fault energy and phase stability of FCC CrMnFeCoNi: an Ab initio study, J. Phase Equilibria Diffus 42 (2021) 551–560, https://doi.org/10.1007/s11669-021-00877-x.
- [60] A.W. Ruff, Measurement of stacking fault energy from dislocation interactions, Metallurg. Trans. 1 (1970) 2391–2413.
- [61] S.J. Lee, Y.S. Jung, S. Il Baik, Y.W. Kim, M. Kang, W. Woo, Y.K. Lee, The effect of nitrogen on the stacking fault energy in Fe-15Mn-2Cr-0.6C-xN twinning-induced plasticity steels, Scr. Mater. 92 (2014) 23–26, https://doi.org/10.1016/j. scriptamet 2014 08 004
- [62] R.P. Reed, R.E. Schramm, Relationship between stacking-fault energy and x-ray measurements of stacking-fault probability and microstrain, J. Appl. Phys. 45 (1974) 4705–4711, https://doi.org/10.1063/1.1663122.
- [63] X.D. Xu, P. Liu, Z. Tang, A. Hirata, S.X. Song, T.G. Nieh, P.K. Liaw, C.T. Liu, M. W. Chen, Transmission electron microscopy characterization of dislocation structure in a face-centered cubic high-entropy alloy Al0.1CoCrFeNi, Acta Mater. 144 (2018) 107–115, https://doi.org/10.1016/j.actamat.2017.10.050.
- [64] D.T. Pierce, J. Bentley, J.A. Jiménez, J.E. Wittig, Stacking fault energy measurements of Fe-Mn-Al-Si austenitic twinning-induced plasticity steels, Scr. Mater. 66 (2012) 753–756, https://doi.org/10.1016/j.scriptamat.2012.01.050.

[65] P.M. Anderson, J.P. Hirth, J. Lothe, Theory of Dislocations, Cambridge University Proce 2017

H.S. Oh et al.

- [66] I. Moravcik, M. Zelený, A. Dlouhy, H. Hadraba, L. Moravcikova-Gouvea, P. Papež, O. Fikar, I. Dlouhy, D. Raabe, Z. Li, Impact of interstitial elements on the stacking fault energy of an equiatomic CoCrNi medium entropy alloy: theory and experiments, Sci. Technol. Adv. Mater. 23 (2022) 376–392, https://doi.org/ 10.1080/14686996.2022.2080512.
- [67] L. Mosecker, A. Saeed-Akbari, Nitrogen in chromium-manganese stainless steels: a review on the evaluation of stacking fault energy by computational thermodynamics, Sci. Technol. Adv. Mater. 14 (2013), https://doi.org/10.1088/ 1468-6996/14/3/033001.
- [68] C. Varvenne, A. Luque, W.A. Curtin, Theory of strengthening in fcc high entropy alloys, Acta Mater. 118 (2016) 164–176, https://doi.org/10.1016/j. actamat. 2016.07.040.
- [69] A. Kosogor, V.A. L'Vov, O. Söderberg, S.P. Hannula, Stabilizing internal stress as the thermodynamic factor of martensite aging effects, Acta Mater. 59 (2011) 3593–3601, https://doi.org/10.1016/j.actamat.2011.02.032.
- [70] K. Otsuka, X. Ren, Mechanism of martensite aging effect, Scr. Mater. 50 (2004) 207–212, https://doi.org/10.1016/j.scriptamat.2003.09.013.
- [71] J. Ding, Q. Yu, M. Asta, R.O. Ritchie, Tunable stacking fault energies by tailoring local chemical order in CrCoNi medium-entropy alloys, Proc. Natl. Acad. Sci. (2018), 201808660, https://doi.org/10.1073/pnas.1808660115.
- [72] Q.J. Li, H. Sheng, E. Ma, Strengthening in multi-principal element alloys with local-chemical-order roughened dislocation pathways, Nat. Commun. 10 (2019) 1–11, https://doi.org/10.1038/s41467-019-11464-7.
- [73] T. Furuhara, Y. Zhang, M. Sato, G. Miyamoto, M. Enoki, H. Ohtani, T. Uesugi, H. Numakura, Sublattice alloy design of high-strength steels: application of clustering and nanoscale precipitation of interstitial and substitutional solutes, Scr. Mater. 223 (2023), https://doi.org/10.1016/j.scriptamat.2022.115063.
- [74] H.L. Che, S. Tong, K.S. Wang, M.K. Lei, M.A.J. Somers, Co-existence of γ'N phase and γN phase on nitrided austenitic Fe–Cr–Ni alloys- I. experiment, Acta Mater. 177 (2019) 35–45, https://doi.org/10.1016/j.actamat.2019.07.019.
- [75] J. Oddershede, T.L. Christiansen, K. Ståhl, M.A.J. Somers, Extended X-ray absorption fine structure investigation of nitrogen stabilized expanded austenite, Scr. Mater. 62 (2010) 290–293, https://doi.org/10.1016/j. scriptamat.2009.11.021.
- [76] K. Tong, F. Ye, Y.K. Wang, Short-range ordered structure and phase stability of supersaturated nitrided layer on austenitic stainless steel, Acta Mater. 175 (2019) 314–323. https://doi.org/10.1016/j.actamat.2019.06.019.

- [77] Y. Benjamini, Y. Hochberg, Controlling the false discovery rate: a practical and powerful approach to multiple testing, J. R. Stat. Soc. Ser. B Stat. Methodol. 57 (1995) 289–300.
- [78] A. Getis, J.K. Ord, The analysis of spatial association by use of distance statistics, Geogr Anal 24 (1992) 189–206, https://doi.org/10.1111/j.1538-4632.1992. tb00261 x
- [79] I. Moravcik, H. Hadraba, L. Li, I. Dlouhy, D. Raabe, Z. Li, Yield strength increase of a CoCrNi medium entropy alloy by interstitial nitrogen doping at maintained ductility, Scr. Mater. 178 (2020) 391–397, https://doi.org/10.1016/j. scriptamat.2019.12.007.
- [80] Y.M. Eggeler, J. Müller, M.S. Titus, A. Suzuki, T.M. Pollock, E. Spiecker, Planar defect formation in the γ' phase during high temperature creep in single crystal CoNi-base superalloys, Acta Mater. 113 (2016) 335–349, https://doi.org/10.1016/j.actamat.2016.03.077.
- [81] M.S. Titus, R.K. Rhein, P.B. Wells, P.C. Dodge, G.B. Viswanathan, M.J. Mills, A. Van Der Ven, T.M. Pollock, Solute segregation and deviation from bulk thermodynamics at nanoscale crystalline defects, n.d. https://www.science.org.
- [82] P. Spatig, J. Bonneville, J.-L. Martin, A new method for activation volume measurements: application to Ni3(A1,Hf), Mater. Sci. Eng. A167 (1993) 73–79.
- [83] T.S. Byun, On the stress dependence of partial dislocation separation and deformation microstructure in austenitic stainless steels, Acta Mater. 51 (2003) 3063–3071, https://doi.org/10.1016/S1359-6454(03)00117-4.
- [84] S. Takaki, H. Nakatsu, Tokunaga Youichi, Effects of austenite grain size on epsilon martensitic transformation in Fe-15mass%Mn alloy, Mater. Trans. 34 (1993) 489–495. JIM.
- [85] A.J. Detor, C.A. Schuh, Grain boundary segregation, chemical ordering and stability of nanocrystalline alloys: atomistic computer simulations in the Ni–W system, Acta Mater. 55 (2007) 4221–4232.
- [86] J. Gao, S. Jiang, H. Zhao, Y. Huang, H. Zhang, S. Wang, G. Wu, Y. Wu, H. Wu, A. Davydov, W.M. Rainforth, Z. Lu, X. Mao, Enhancing strength and ductility in a near medium Mn austenitic steel via multiple deformation mechanisms through nanoprecipitation, Acta Mater. (2023) 243, https://doi.org/10.1016/j.actamat.2022.118538
- [87] A. Abu-Odeh, M. Asta, Modeling the effect of short-range order on cross-slip in an FCC solid solution, Acta Mater. 226 (2022), https://doi.org/10.1016/j. actamat.2021.117615.
- [88] H. Wei, Y. Wei, Interaction between a screw dislocation and stacking faults in FCC metals, Mater. Sci. Eng. A 541 (2012) 38–44, https://doi.org/10.1016/j.msea.2012.01.115.